

MAPPING THE HYPORHEIC ZONE IN AN ACID-ROCK IMPACTED STREAM WITH A  
SALT TRACER AND ELECTRICAL RESISTIVITY IMAGING UNDER  
GAINING AND LOSING CONDITIONS

By

Dayana A. Arrue

A thesis submitted to the Faculty and the Board of Trustees of the Colorado School of Mines in partial fulfillment of the requirements for the degree of Master of Science (Hydrology).

Golden, Colorado

Date \_\_\_\_\_

Signed: \_\_\_\_\_  
Dayana A. Arrue

Signed: \_\_\_\_\_  
Dr. Kamini Singha  
Thesis Advisor

Golden, Colorado

Date \_\_\_\_\_

Signed: \_\_\_\_\_  
Dr. David Benson  
Professor and Director  
Hydrologic Science and Engineering Program

## ABSTRACT

Acid-mine drainage (AMD) from legacy mining and acid-rock drainage (ARD) from sulfide-rich bedrock geology degrades water quality and aquatic habitat by sourcing low pH, metal-laden water to streams. The hyporheic zone serves as a biogeochemical hotspot in numerous streams impacted by acid mine drainage, where it helps regulate metal(loid) reactions and enhances water quality by causing the precipitation of metal oxides capable of adsorbing toxic metal(loid)s. Here, we used time-lapse electrical resistivity imaging and constant-rate sodium chloride tracer injections to assess the extent of the hyporheic zone in a high-alpine stream, Coal Creek, near Crested Butte, Colorado. This stream has been impacted by historic mining, AMD, and metal loads naturally originating from bedrock and fracture zones (i.e., ARD). Two tracer injection tests were performed during baseflow at similar flow rates, one during localized losing stream conditions and the other during localized gaining stream conditions. Electrical resistivity imaging, fluid (surface water), groundwater, and bulk electrical conductivities, and surface water and groundwater elevations and temperatures were analyzed to characterize surface water-groundwater interactions with the goal of delineating the hyporheic zone and its potential influence on metal fate and transport in Coal Creek, a snowmelt-dominated watershed. Results indicated that the hyporheic zone is constrained to ~2.5m below the stream and the immediate banks with a slight connectivity to an adjacent floodplain during the August baseflow tracer test under gaining stream conditions. In contrast, the hyporheic zone was constrained to ~2m below the stream and the immediate banks during the September baseflow tracer test under losing stream conditions. In general, the hyporheic zone had only minimal differences between tests and its overall impact to the stream system is similar during both conditions. The bulk conductivity revealed a diel cycle that mimicked groundwater temperature

during both tracer tests. Based on the fluid and bulk breakthrough curves, the tracer's transport was largely unhindered by transport through the hyporheic zone under both conditions, and there was no conclusive trend found between the stream condition (losing versus gaining) and the percent mass recovery, mean arrival time, variance, and skewness, which were calculated with temporal moments. Our results indicate metals in this system would therefore be driven largely by advection and dispersion with minimal retardation by transient storage through this stream system at baseflow. The hyporheic zone consequently has minimal capacity to attenuate metals along the studied reach during baseflow conditions, and metal loading into Coal Creek is expected to degrade downstream water quality.

## TABLE OF CONTENTS

ABSTRACT .....	iii
LIST OF FIGURES .....	vii
LIST OF TABLES.....	x
LIST OF EQUATIONS .....	xi
ACKNOWLEDGEMENTS.....	xii
CHAPTER 1 GENERAL INTRODUCTION .....	1
CHAPTER 2 MAPPING THE HYPORHEIC ZONE IN AN ACID-ROCK IMPACTED STREAM WITH A SALT TRACER AND ELECTRICAL RESISTIVITY IMAGING UNDER GAINING AND LOSING CONDITIONS.....	4
2.1 Abstract.....	4
2.2 Introduction.....	5
2.3 Study Site.....	8
2.4 Methods.....	12
2.4.1 Constant-Rate Stream Tracer Injection.....	12
2.4.2 August Tracer Test.....	14
2.4.3 September Tracer Test .....	15
2.4.4 Temporal Moments for Time-Series Analysis.....	16
2.5 Results and Discussion .....	18
2.5.1 Water Levels .....	18
2.5.2 Temperature .....	19
2.5.3 Background Surface Water and Groundwater Specific Conductivity .....	20
2.5.4 Fluid and Bulk Conductivity Breakthrough Curves .....	21
2.5.5 Zeroth Temporal Moment: Solute Mass Breakthrough Curves.....	22
2.5.6 Inversion of Resistivity Data .....	26
2.5.7 Implication of Results.....	31
2.6 Conclusions.....	32

CHAPTER 3 FUTURE WORK .....	34
3.1 Tracer tests at higher discharge.....	34
3.2 Tracer mass .....	34
3.3 Equipment.....	34
3.4 Data collection .....	35
3.5 Geochemistry Sampling.....	35
3.6 Gaining and Losing Stream Measurements .....	35
3.7 Fiber Optic Distributed Temperature Sensing .....	36
3.8 Coupled Modeling .....	36
REFERENCES .....	37
APPENDIX A SUPPORTING FIGURES AND ANALYSES.....	44
APPENDIX B SUPPLEMENTAL FILES .....	51
B.1 August Electrical Resistivity Tracer Inversions .....	51
B.2 September Electrical Resistivity Tracer Inversions.....	51
B.3 Tracer Test Data From 2300m Injection Site .....	51

## LIST OF FIGURES

Figure 1.1: Conceptual model of the hyporheic zone: location at streambeds and banks where ground water interacts with the surface water (U.S. Geological Survey, 2016). .....	2
Figure 1.2: Conceptual models of (A) losing and (B) gaining stream conditions (U.S. Geological Survey, 2016). .....	3
Figure 2.1: A) The study area is located along a 3-km reach of the Coal Creek watershed in the central Rocky Mountains region of Gunnison County, Colorado. The study reach is highlighted in the red rectangle in A), the Mt. Emmons treatment plant’s location is shown by the solid red circle, the orange triangle represents the stream gauge managed by the U.S. Geological Survey at Coal Creek (Gage #09111250), and the three neighboring mines are also represented by diamonds of different colors: Forest Queen, Standard, and Keystone mines. The water flow is in the easterly direction. B) The study area is shown along with its geology and the locations of the electrical conductivity loggers and pressure transducers, injection point, and the ER transect. The yellow geological features are unconsolidated surficial deposits, and the pink features indicate consolidated rocks including granodiorite and quartz. A large fracture is also shown on the map. C) The relative elevation and relative horizontal distances between the electrodes from the ER transect are shown, where the zero elevation was randomly selected to be electrode # 17 .....	9
Figure 2.2: Stream discharge measured at the USGS station (Gauge #09111250, shown in Figure 2.1A) from March to December of 2022. The times at which the tracer tests and ER surveys were performed are shown on the graph .....	14
Figure 2.3: Data measured with a pressure transducer through time since injection start in wells upstream of the injection site, including the SW and GW elevations in A) August and B) September, and SW and GW temperatures in C) August and D) September. ....	19
Figure 2.4: The SW and GW specific conductivity, as measured at the background loggers upstream of the injection point (Figure 2.1C) during the A) August and B) September tracer injection tests. ....	20
Figure 2.5: The non-normalized bulk conductivity and fluid conductivity measured 100 m downstream of the injection over time since injection during the A) August tracer test and the B) September tracer test.. ....	22
Figure 2.6: Surface water BTCs measured at A) 100m, 250m, and 2300m downstream from the injection site during the August tracer experiment and B) 100m, 250m, 1080m, and 2300m downstream from the injection site during the September tracer experiments, with percent of mass recovery shown within each curve. The	

mass injected was 45 kg for August and 68 kg for September. The BTCs are shown as NaCl concentrations (as calculated from the specific conductivity). Note issues during the August test at the 100 m location, where the background-adjusted concentration reached negative values, possibly because the sensor was not fully submerged for the entirety of the tracer test. ....25

Figure 2.7: Cross-sectional ER inversions from August, with stream flow directed out of the page. A) The pre-injection electrical resistivity model with distance (m) in the x-axis and elevation on the y-axis (m). Areas of high resistivity (the cobble-bed stream at X=5-8 m and the floodplain at X=18-25 m) are likely preferred flowpaths, based on changes in ER shown below. B) The diagonal of the resolution matrix, which measures how well the model parameters are resolved by the data, i.e., a value close to 1 would indicate perfect model resolution from data. The dashed line is the depth of investigation (DOI). C–H) Selected ER inversions for the tracer injection test (see Appendix B for all images) as percent changes from the pre-injection electrical resistivity model at time elapsed from the start of tracer injection. ....29

Figure 2.8: Inversion models from September are presented as cross-sections transverse to the stream with stream flow directed out of the page. A) The pre-injection electrical resistivity model with distance (m) in the x-axis and elevation on the y-axis (m). B) The diagonal of the true resolution matrix, which measures how well the data and the model parameters are resolved i.e., any resolution value close to 1 would indicate equal predicted and measured values. The dashed line is the depth of investigation (DOI). C–H) Selected ER inversions for the tracer injection test (see Appendix B for all images) as percent changes from the pre-injection electrical resistivity model at time elapsed after beginning the conservative solute injection. C–G) Decrease in bulk resistivity in the subsurface due to tracer presence. H) The tracer is flushed from the subsurface.....30

Figure A.1: Select data from the (A-C) August and (D-F) September 2022 tracer injection experiments showing the SW and GW relative elevation as measured (A, D) immediately upstream of the injection site, and (B, E) 1080m and (C, F) 2300m downstream of the injection site —with a pressure transducer—over time since injection start. ....44

Figure A.2: The GW temperatures and bulk conductivities during the (A) August and (B) September tracer tests over time since the start of injection. ....45

Figure A.3: Hysteresis patterns measured during the September tracer experiment 100m downstream from the injection site. This shows the associated hinge points used to determine  $\beta$  from the rising limb (injection phase) as outlined by Briggs et al. (2014).....46

Figure A.4: The equations presented by Briggs et al. (2014) on how to yield estimates of the ratio of less mobile to mobile porosities ( $\beta$ ) using the graphical method.....46

Figure A.5: Select data used for processing the ER data collected during the (A-D) August tracer test and the (E-H) September tracer test, including (A, E) measured apparent resistivity, the (B, F) conductivity as measured by the IRIS instrument, the (C, G) calculated resistivity and (D, H) calculated conductivity.....47

Figure A.6: Temporal moments were calculated based on the fluid conductivity at the four downstream locations (100, 250, 1080 and 2300 m) and based on bulk conductivity at 100 m downstream from the injection, during two different baseflow conditions (gaining in August and losing in September). The temporal moments were used to determine (A, E) percent mass recovery (%), (B, F) mean arrival time (hr), (C, G) temporal variance ( $hr^2$ ), and (D, H) skewness ( $hr^3$ ). Note the skewness values shown in purple in the D subplot correspond to the 2300 m location. Additionally, skew values for each downstream location were not truncated to represent equal times after injection start, but were taken according to each time length as shown in Figure 2.6 .....48

Figure B.1: A) From top to bottom: for the August tracer (A) measured apparent resistivity and the (B) conductivity as measured by the IRIS instrument are compared to the (C) calculated resistivity and (D) calculated conductivity. ....54

Figure B.2: A) The bulk versus fluid conductivity for the August tracer test performed 2300m downstream.....54

Figure B.3: Inversion models from August at the 2300m location are presented as cross-sections transverse to the stream with flow directed out of the page. A) The pre-injection electrical resistivity model. B) The diagonal of the true resolution matrix, which measures how well the data and the model parameters are resolved i.e., any resolution value close to 1 would indicate equal predicted and measured values. The dashed line is the depth of investigation (DOI). C–H) Selected ER inversions for the tracer injection test (see Appendix B for all images) as percent changes from the pre-injection electrical resistivity model at time elapsed after beginning the conservative solute injection. C–G) Decrease in bulk resistivity in the subsurface due to tracer presence. H) Tracer is flushed from the subsurface .....54

LIST OF TABLES

Table 2.1: The recovered mass in kilograms and as a percentage in the stream as calculated for each downstream location using the zeroth moment. The total mass of tracer injected for each tracer test is also shown. The mass injected was 45 kg for August and 68 kg for September. NC indicates data was “not collected.” .....26

## LIST OF EQUATIONS

EQ 2.1	Specific Conductance Equation.....	16
EQ 2.2	The nth Order of a Temporal Moment Equation .....	17
EQ 2.3	Keller and Frischknecht (1966) Observed Solute Mass Equation.....	17
EQ 2.4	Solute Mass Estimate Equation .....	17
EQ 2.5	First Central Moment Equation .....	17
EQ 2.6	Second Central Moment Equation.....	17
EQ 2.7	Third Central Moment Equation.....	17

## ACKNOWLEDGEMENTS

This work would not have been possible without funding from the Jack Kent Cooke Foundation, who not only provided support, guidance, and financial assistance, but also encouraged me to dream big. I would like to thank Dr. Kamini Singha, my advisor, for believing in me and granting me the opportunity to conduct the research presented in this thesis. Her guidance has been invaluable, and she has challenged me to broaden my scientific horizons and acquire new technical skills. I also extend my appreciation to my committee members, Dr. Alexis Sitchler and Dr. Manika Prasad, for their perspectives that contributed to this research. I am thankful to the Mines professors and faculty members who shared their knowledge and professional experiences. I am equally grateful to my classmates and fellow students at Colorado School of Mines for providing feedback on research, clarifying concepts in class, and offering support through the graduate school journey. Finally, I am thankful for my supportive girlfriend, family, and friends, whose encouragement has been a source of motivation throughout my time at Mines.

Dedicated to my beloved mother, Candida Arrue, whose unwavering love, strength, and support empower me to pursue the desires of my heart.

## CHAPTER 1

### GENERAL INTRODUCTION

Mountainous water resources in the western United States play an important role in supporting drinking water systems, irrigation, hydropower, and local economies, among other activities. However, these resources are increasingly vulnerable due to climate change, and, in many places, the impacts of acid mine drainage (AMD) and acid rock drainage (ARD). The western U.S. is already in a record-breaking megadrought that affects the region's freshwater supply and with numerous abandoned mines in the western U.S., the leaching of mine waste into surface water and groundwater has become a significant concern in part due to AMD. AMD occurs when sulfide minerals oxidize and release metal-heavy, low-pH water into the environment. Understanding the fate and transport of metals in these impacted ecosystems is important, especially in the context of a changing climate.

The hyporheic zone, an area in the subsurface around streams where groundwater and surface waters mix (Figure 1.1), can help by regulating metal reactions and improving water quality in AMD-impacted streams. The hyporheic zone is known as a biogeochemical hotspot where movement of metals is delayed and processes inducing compounds (e.g., metal ions) to change from solution to a solid phase and become incorporated within a larger growing solid may take place (i.e., precipitation and sorption processes). Additionally, the hyporheic zone is vital for providing habitats for organisms, moderating temperatures, and cycling energy, nutrients, and organic compounds for an overall improvement in water quality. Quantifying the controls affecting movement and storage within the hyporheic zone is essential for understanding metal fate and transport in streams, including those impacted by AMD.

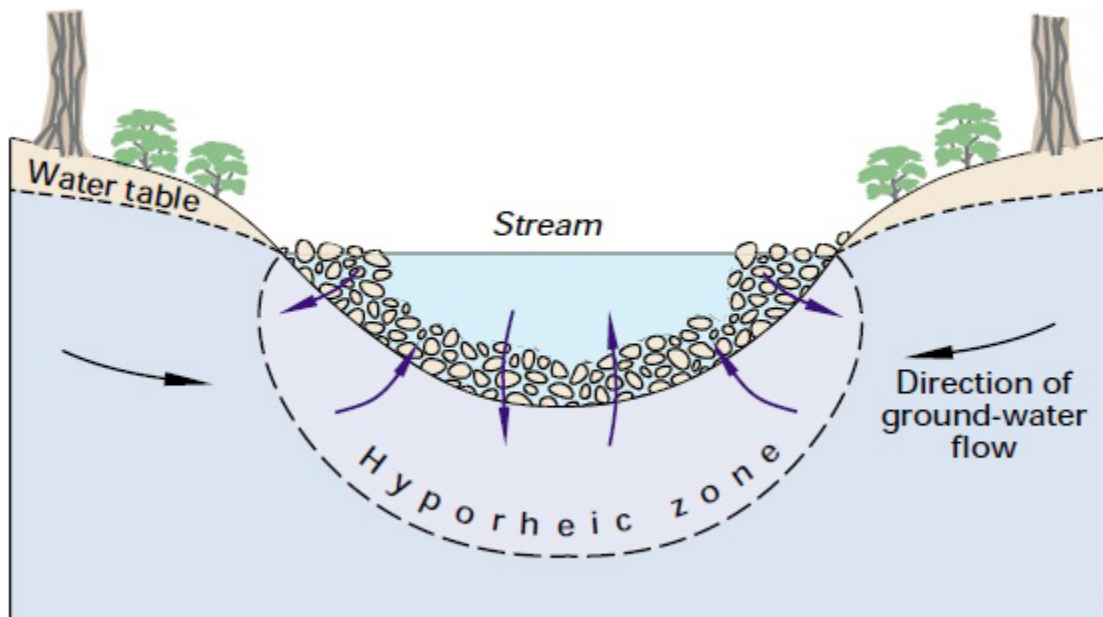


Figure 1.1: Conceptual model of the hyporheic zone: location at streambeds and banks where ground water interacts with the surface water (U.S. Geological Survey, 2016).

Various field-measurement methods have historically been used to investigate the hyporheic zone. In this study, we performed salt tracer injections at a constant rate and employed a geophysical method, specifically electrical resistivity, to determine the hyporheic zone area and processes affecting the transfer of mass between surface water and groundwater. Electrical resistivity surveys are surface-based and work by injecting an electrical current into the ground through electrodes (e.g., 20-cm steel rods) and measuring the resulting voltage difference at other electrodes. Then, the voltage difference is used to map out the electrical resistivity values of the subsurface materials in a cross-section. Electrical resistivity is inversely related to electrical conductivity and is indicative of conductive materials in the subsurface such as metals and ions in fluids. Salts and other chemicals that dissolve in the surface water or groundwater increase the electrical conductivity and is the reason salt tracers are used when identifying flowpaths. Here, we perform the electrical resistivity surveys specifically under different flow conditions between the

stream and aquifer: losing and gaining (Figure 1.2). A stream is considered losing when the water elevation in the stream is higher than that of the surrounding groundwater, resulting in a net outflow of water from the stream to the groundwater. A gaining stream describes a net inflow from groundwater because the stream's water elevation is lower than that of the groundwater. Our goals are to better understand the potential of the hyporheic zone to influence the overall water quality and the movement of metals in the Coal Creek Watershed near Crested Butte, Colorado. This work is important because Coal Creek serves as the main water source for the town of Crested Butte; however, its susceptibility to climate change and elevated metal loading due to its metal-rich geology and mining legacy make it an important site to assess the dynamic processes influencing its water quality.

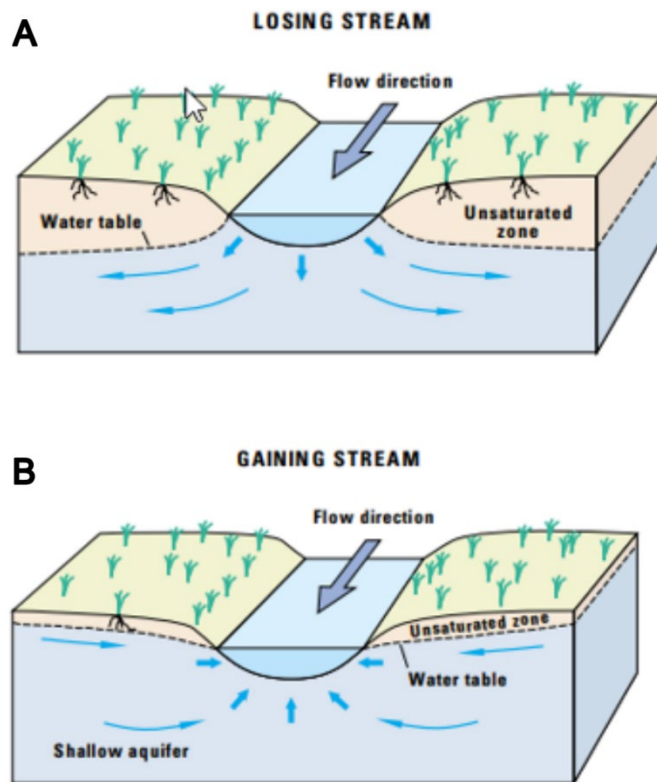


Figure 1.2: Conceptual models of (A) losing and (B) gaining stream conditions (U.S. Geological Survey, 2016).

## CHAPTER 2

# MAPPING THE HYPORHEIC ZONE IN AN ACID-ROCK IMPACTED STREAM WITH A SALT TRACER AND ELECTRICAL RESISTIVITY IMAGING UNDER GAINING AND LOSING CONDITIONS

### 2.1.1 Abstract

Acid-mine drainage (AMD) from legacy mining and acid-rock drainage (ARD) from sulfide-rich bedrock geology degrades water quality and aquatic habitat by sourcing low pH, metal-laden water to streams. The hyporheic zone serves as a biogeochemical hotspot in numerous streams impacted by acid mine drainage, where it helps regulate metal(loid) reactions and enhances water quality by causing the precipitation of metal oxides capable of adsorbing toxic metal(loid)s. Here, we used time-lapse electrical resistivity imaging and constant-rate sodium chloride tracer injections to assess the extent of the hyporheic zone in a high-alpine stream, Coal Creek, near Crested Butte, Colorado. This stream has been impacted by historic mining, AMD, and metal loads naturally originating from bedrock and fracture zones (i.e., ARD). Two tracer injection tests were performed during baseflow at similar flow rates, one during localized losing stream conditions and the other during localized gaining stream conditions. Electrical resistivity imaging, fluid (surface water) and bulk electrical conductivities, and surface water and groundwater elevations and temperatures were analyzed to characterize surface water-groundwater interactions with the goal of delineating the hyporheic zone and its potential influence on metal fate and transport in Coal Creek, a snowmelt-dominated watershed. Results indicated that the hyporheic zone is constrained to 2 to 2.5 m below the stream and the immediate banks with a slight connectivity to an adjacent floodplain during tracer tests during the two

differing localized flow regimes. The bulk conductivity revealed a diel cycle that mimicked groundwater temperature during both tracer tests. Based on the fluid and bulk breakthrough curves, the tracer's transport was largely unhindered by transport through the hyporheic zone under both conditions, and there was no conclusive trend found between the stream condition (losing versus gaining) and the percent mass recovery, mean arrival time, variance, and skewness, which were calculated with temporal moments. Our results indicate metals in this system would therefore be driven largely by advection and dispersion with minimal retardation by transient storage through this stream system at baseflow. The hyporheic zone consequently has minimal capacity to attenuate metals along the studied reach during baseflow conditions, and metal loading into Coal Creek is expected to degrade downstream water quality.

### **2.1.2 Introduction**

Water in the western United States is limited, and streams are crucial resources supplying domestic drinking water, irrigation water, hydropower, and economic value to many western communities. The impacts of climate change on high-alpine areas in the western U.S. are increasingly concerning due to a record-breaking megadrought, which is affecting the region's freshwater supply that relies heavily on snowmelt runoff (Hrozencik, 2021; Williams et al., 2022). High-alpine areas are remote, steep, and rely on snowmelt for freshwater. Studies exploring snowmelt-driven runoff in the western U.S. mountains show shifts in the winter snow-driven runoff season that lead to changes in water availability in the region (McCabe & Clark, 2005; Rauscher et al., 2008). Water availability over the mountainous U.S. is expected to decrease as winter flows increase due to an increasing global temperature (Coppola et al., 2018). Climate change also impacts mountain stream ecosystems, including snowmelt timing and stream thermal dynamics (Brown et al., 2006). These freshwater systems are crucial as drinking water sources

and drivers of economic activity, including tourism in local mountain towns and the downstream regions (Shanklin & Ryan, 2006; Hood & Hayashi, 2015).

Acid mine drainage (AMD) and acid rock drainage (ARD) are other acute stressors on mountainous freshwater streams (Dennehy et al., 1993; Clements et al., 2000; Niyogi et al., 2002; DeGraff, 2007; USEPA, 2020). AMD and ARD are generated when a sulfide mineral is oxidized, generating acid and releasing low-pH, metal-laden water to the environment. Mine waste is prevalent in the western U.S. and leaches into surface water (SW) and groundwater (GW). The Mineral Policy Center notes that there are 557,000 abandoned mines in the U.S. (The Mineral Policy, 1994), estimated to affect 26,000 km of streams in the western U.S. (DeGraff, 2007) and approximately 600 km in Colorado alone (Wentz, 1973; Shanklin & Ryan, 2006). Consequently, it has become a priority for scientists to better measure the controls of metal fate and transport in these ecosystems (Cochand et al., 2019; Fields & Dethier, 2019; Zhi et al., 2020; Heil et al., 2022), especially under a changing climate where stressors on water availability are projected to increase.

In many AMD-impacted stream systems, the hyporheic zone is a biogeochemical hot spot that regulates metal(loid) reactions and improves water quality through precipitation of metal oxides that can sorb toxic metal(loid)s (Fuller & Harvey, 2000; Hoagland et al., 2020). The hyporheic zone is the interface where SW encounters shallow GW and is defined by the interactions and exchanges that are crucial for the overall stream system's health. The hyporheic zone was termed "the river's liver" (Fischer et al., 2005) due to its significance for carbon and nitrogen cycling. It is vital for providing habitats for organisms, moderating temperatures, and cycling energy, nutrients, and organic compounds for an overall improvement in water quality (Boulton et al., 1998; Fischer et al., 2005; Cardenas, 2015; Magliozzi et al., 2018). In many

mountainous regions where AMD is common, the hyporheic zone is important for releasing or attenuating metal contaminants (Gandy et al., 2007). The hyporheic zone can act as a buffer, delaying the movement of contaminants from SW to GW or vice versa (Benner et al., 1995); the travel time along hyporheic flowpaths is a primary control on biogeochemical cycling (Boano et al., 2010; Zarnetske et al., 2012). There are also instances where reaction or sorption sites in the hyporheic zone may lead to the accumulation of contaminants to zones where they can be more easily removed (Fuller & Harvey, 2000). Quantifying controls on storage area and mass transfer within the hyporheic zone remains a key challenge to delineate metal fate and transport in streams.

Several field-measurement methods have been used to determine the presence, extent, and flow through the hyporheic zone. Seepage meters, mini-piezometers, and thermal sensors have been employed to estimate hyporheic exchange flow (e.g., Lewandowski et al., 2019). Another common method includes the injection of a conservative tracer into the stream while collecting samples downstream to measure a breakthrough curve (BTC) that is a function of downstream transport, tracer flow paths, and SW-GW exchange (Harvey & Gorelick, 1995; Gooseff et al., 2008; Ward et al., 2010b). Additionally, geophysical methods can be beneficial for determining the spatial extent of the hyporheic zone and how hydrogeological characteristics impact the SW-GW exchange (Singha et al., 2008; Gaona et al., 2019). Time-lapse electrical resistivity (ER) imaging has been useful for mapping hyporheic exchange during tracer injections. Geophysics can be utilized to conceptualize dual-domain mass transfer processes in aquifers as well as the area of exchange between the stream and surrounding aquifer (Singha et al., 2008; Doetsch et al., 2012; Ward et al., 2014; Singley et al., 2022).

Here, we look to use ER in conjunction with saline tracers to determine the extent of the hyporheic zone in a metal-impacted reach in Coal Creek, in western Colorado, to determine the role of the hyporheic zone in this system and its potential to attenuate the metal loading into the stream. Discharge relations on hyporheic flow have been studied—longer hyporheic residence times under low-flow conditions promote sorption, precipitation, and other biogeochemical reactions in the hyporheic zone, resulting in retention and accumulation of metals (Trévisan & Perriñez, 2016). That said, it is less clear how locally gaining and losing stream conditions might affect hyporheic efficacy. Previous studies have shown that both gaining and losing flows ultimately restrict hyporheic exchange flow because they prevent stream water from penetrating the streambed and stream banks (Boano et al., 2008; Lewandowski et al., 2019). So for this work, we ask the question: do local gaining or losing conditions change the size and efficacy of the hyporheic zone for processing metals? An analysis during these two conditions will quantify how varying hydrologic conditions influence hyporheic zone extent and capacity to mediate biogeochemical reactions during similar flow conditions.

### **2.1.3 Study Site**

This study focuses on the Coal Creek watershed, located in Gunnison County, Colorado, near Crested Butte, CO (Figure 2.1A). Coal Creek is a high-alpine, snowmelt-dominated watershed where legacy mining from the Ruby Mining District and metal-rich geology have resulted in elevated metal loading to the stream. Coal Creek is also the main water supply for the roughly 1500 people residing in the Town of Crested Butte (Ryan et al., 2009).

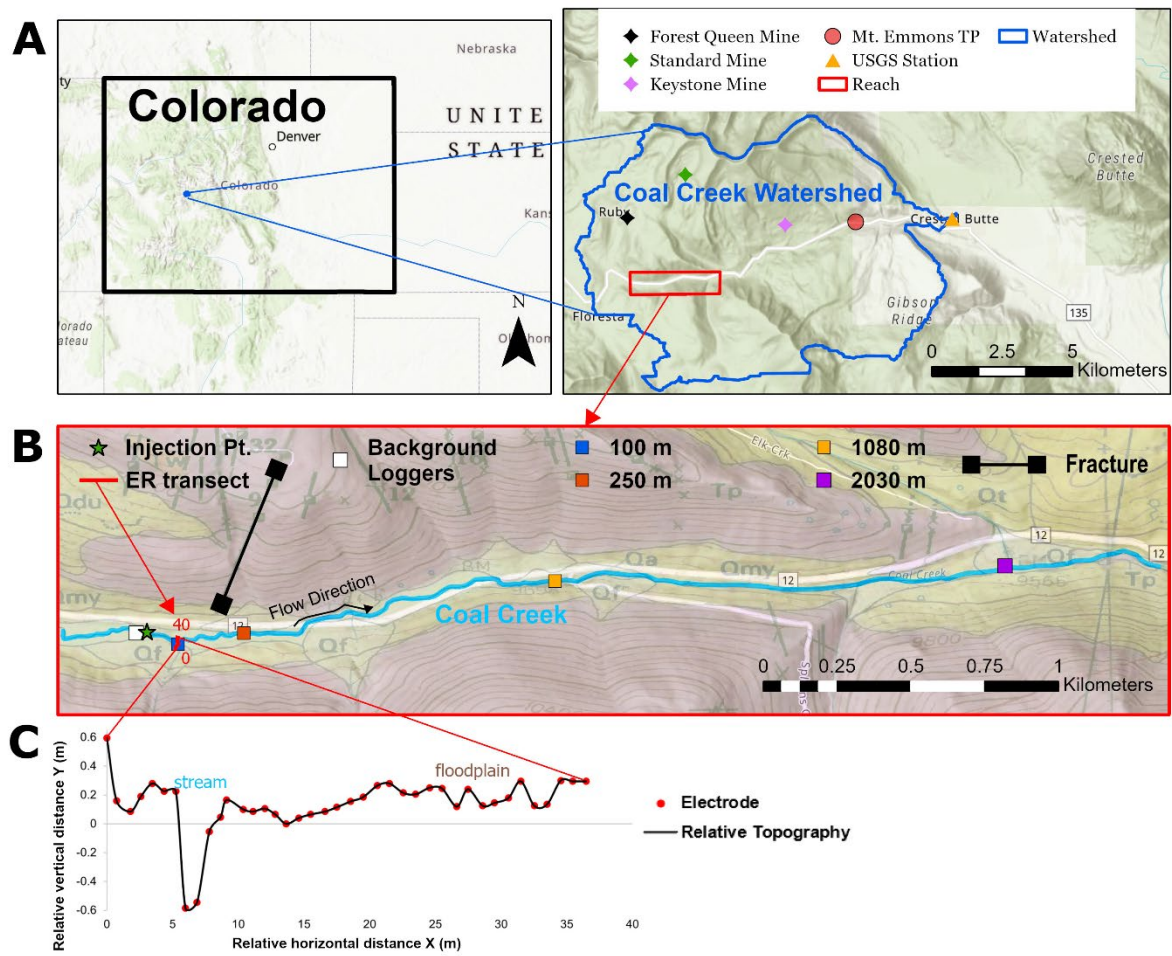


Figure 2.1: A) The study area is located along a 3-km reach of the Coal Creek watershed in the central Rocky Mountains region of Gunnison County, Colorado. The study reach is highlighted in the red rectangle in A), the Mt. Emmons treatment plant’s location is shown by the solid red circle, the orange triangle represents the stream gauge managed by the U.S. Geological Survey at Coal Creek (Gage #09111250), and the three neighboring mines are also represented by diamonds of different colors: Forest Queen, Standard, and Keystone mines. The water flow is in the easterly direction. B) The study area is shown along with its geology and the locations of the electrical conductivity loggers and pressure transducers, injection point, and the ER transect. The yellow geological features are unconsolidated surficial deposits, and the pink features indicate consolidated rocks including granodiorite and quartz. A large fracture is also shown on the map. C) The relative elevation and relative horizontal distances between the electrodes from the ER transect are shown, where the zero elevation was randomly selected to be electrode # 17.

Coal Creek is a third-order, meandering stream with a cobbly bed that drains an area of approximately 53 km<sup>2</sup> and ranges in elevation from 2700 m to 3700 m. The reported average

slope is approximately 16 degrees (Zhi et al., 2019). Stream flow in this watershed is dominated by snowmelt, and flow precedes from west to east through the town of Crested Butte, eventually draining into the East River (Figure 2.1A). There is one stream gauge managed by the U.S. Geological Survey at Coal Creek: Gauge #09111250, which is in the Town of Crested Butte and has been monitored since 2014.

The geology of the area includes alluvial deposits in the Coal Creek valley, with laccoliths and Mesa Verde sandstone forming the mountains surrounding the valley (Gaskill et al., 1987). Bedrock geology contains vein deposits rich in copper, gold, lead, molybdenum, ruby, silver, and zinc (Streufert et al., 1999). Legacy mines in the area include the Standard Mine, the Keystone Mine, and the Forest Queen Mine (Figure 2.1A). Sources of metal and acidity to Coal Creek include the Standard Mine, a natural iron gossan and fen, and from a gulch downstream of Forest Queen Mine (Shanklin & Ryan, 2006; Ryan & Bevan, 2009, 2009). AMD and ARD in this area reach the stream mostly through subsurface transport. As stream pH increases, metals precipitate from the water column onto the streambed downstream of the AMD inputs (Kerndorff & Schnitzer, 1980; Lee et al., 2002). In a study conducted in 2005 and 2006, it was found that the Mt. Emmons Treatment Plant (TP), which is located downstream of the Keystone Mine (Figure 2.1A), contributed calcium seven times greater than the background levels. Also, chronic aquatic life toxicity standards were exceeded by several metals downstream of Elk Creek, which carries discharge from the Standard mine into Coal Creek and the iron gossan tributary west of the Standard Mine; however, drinking water supply standards were not exceeded. The Standard Mine was determined to be a Superfund Site, but its drainage has been treated at the Mount Emmons treatment facility since 1981 (Shanklin & Ryan, 2006). The U.S. Environmental Protection Agency (EPA) has performed soil and waste rock/tailings and SW remediation actions since 2006

and to our knowledge, continue to present (USEPA, 2020). The EPA is currently monitoring the remedial course of action and systems implemented through water and soil quality evaluations.

Two constant-rate tracer injection stream experiments were performed in the Coal Creek watershed in August and September of 2022 along a 3-km stream reach (Figure 2.1B) upstream of previous studies near the Standard Mine and the Keystone Mine. An ER survey was performed downstream of the injection site to spatially determine the extent, if present, of the hyporheic zone (Figure 2.1B, 2.1C). The tracer injection site is located at the western end of the catchment (Figure 2.1A) and is within the stream valley. Stream width varies from 2.5 - 4 m during baseflow, and vegetation near the stream is composed of willows, spruce trees, grasses, and bushes. This section of the watershed is comprised of granodiorite porphyry bedrock, which is expected to be a regional source of metal(loids) and is also downgradient from a fracture zone that may drive loading of metal-laden groundwater. We expect a difference in water chemistry in these upstream sites, where the underlying bedrock has naturally occurring high-metal concentrations from fracture zones compared to the downstream Coal Creek extents where the underlying bedrock is sedimentary Mesa Verde sandstone, which is not expected to have significant naturally occurring metal concentrations. Unlike previous studies at the Coal Creek watershed that explored the impacts from mining activities, our study focuses on an upstream reach downgradient from a fracture zone that may drive naturally occurring loading of metal-laden groundwater as a regional source of metal(loids). The August tracer test was performed during gaining stream conditions while the September test was performed during losing stream conditions. The injection site has a stream width ranging from 1 to 3 m with rocks ranging from pebbles to medium-sized cobbles in the streambed.

## 2.1.4 Methods

Our experiments consist of two constant rate stream-tracer injections during baseflow. The tracer tests were performed in August during locally gaining stream conditions and in September during locally losing stream conditions. Temporal moments analyses were used to analyze solute transport within the study reach. An ER survey was also employed during each tracer and the open-software ResIPy was used to invert the ER time series data. Details are below.

### 2.4.1 Constant-Rate Stream Tracer Injection

The stream discharge during both tracer experiments were near baseflow conditions (Figure 2.1). The ionic tracer used in this study was sodium chloride (table salt) mixed with stream water. The goal was to increase background concentrations by approximately  $100 \mu\text{S}/\text{cm}$  above background conditions of approximately  $90 \mu\text{S}/\text{cm}$ . The tracer solution was continuously pumped into Coal Creek over  $\sim 4.5$  hours, and a mechanical in-line flow meter was used to monitor the desired injection rate. The tracer injection rate of  $\sim 1 \text{ L}/\text{min}$  and mixing zone distances of 100m were calculated based on measured stream discharge rates and the modified advection-dispersion equation (González-Pinzón et al., 2022). Fluid conductivity measurements were collected prior, during, and post tracer injection with loggers (HOBO U-24, Onset Computing). An upstream conductivity logger was used to record stream and groundwater background readings during the injection, fluid electrical conductivity (EC) was also measured at three locations downstream from the injection point during the August tracer experiment and at four locations downstream of the injection point during the September tracer test (Figure 2.1B). The fluid conductivity was collected at each logger location prior to the start of the injection and was subtracted from each observation during the tracer test to isolate the signal of the tracer from background conditions. To determine the concentration of the ionic tracer in  $\text{mg}/\text{L}$ , the specific

conductivity measured from the transducers in  $\mu\text{S}/\text{cm}$  was multiplied by a factor of 0.5 based on literature estimates (Keller and Frischknecht, 1966).

The SW and GW temperatures and elevations, relative to the streambed, were collected using pressure transducers (HOBO U-20L, Onset Computing), which were located with the background loggers, immediately upstream of the injection point (Figure 2.1B). An air pressure transducer was located 2300m downstream of the injection point and this was used to obtain absolute pressure as a reference for calculating GW and SW elevation. Collection of SW and GW levels, temperature, and EC were used to quantify SW-GW interactions and flow direction (i.e., gaining vs. losing conditions). SW and GW elevations were also collected downstream of the injection point and these results may be found in Appendix A.

ER data were collected via a perpendicular transect to the stream at a distance downstream of the estimated mixing zone (Figure 2.1B, C). The ER imaging allows for the spatially distributed assessment of solute transport in the subsurface, highlights spatial and temporal dynamics of SW-GW interactions, and allows us to explore the importance of hyporheic zone in regulating metal fate and transport. The ER transects were composed of 40 electrodes at a 1-m spacing perpendicular to the stream. Relative electrode locations and elevation profiles were collected using an auto-level and a Trimble Geo 7X RTK global positioning system with a Zephyr 3 antenna. The ER data were collected with an IRIS Syscal Pro Resistivity Meter using a dipole-dipole geometry with 437 quadripoles (Figure 2.1C). Each dataset took approximately 16 minutes to collect. This setup allowed for a shallow penetration depth, important for capturing the hyporheic zone with high spatial and temporal resolution. The inversion of the ER data was completed in ResIPy (Blanchy et al., 2020). Data weights in the inversion were based on stacking errors as well as a modeling error calculated by ResIPy. The time-lapse inversion capability of

ResIPy allowed for the plotting of percent differences in bulk resistivities from before the tracer injection with values during and after the tracer injection. These inversion models were analyzed for the location and extent of the hyporheic zone, and the timing of subsurface and instream tracer breakthrough. Appendix B shows the final root-mean-square error (RMSE) for the August and September ER inversions, respectively. Below, we outline the details of our two tracer tests.

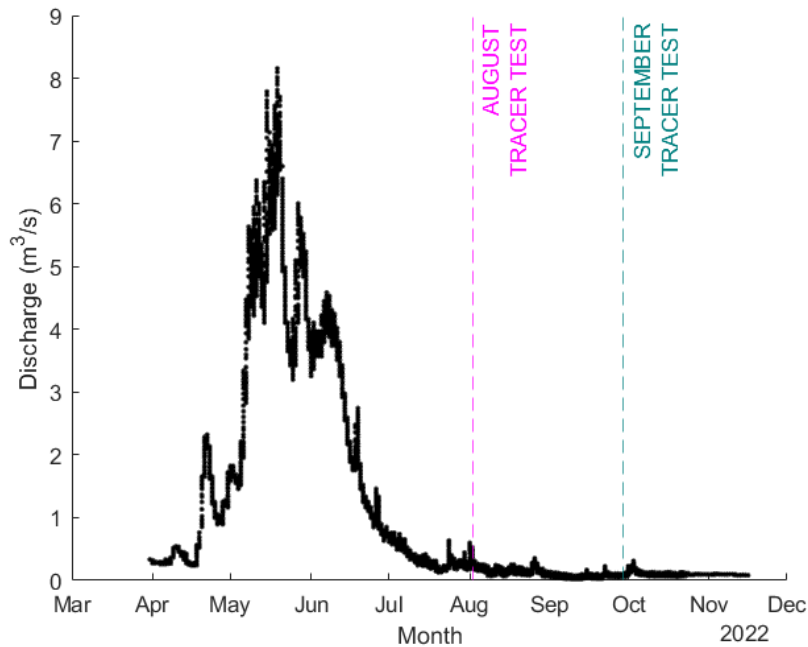


Figure 2.2: Stream discharge measured at the USGS station (Gauge #09111250, shown in Figure 2.1A) from March to December of 2022. The times at which the tracer tests and ER surveys were performed are shown on the graph.

### 2.4.2 August Tracer Test

The average air temperature for the August 2, 2022 tracer test was 15.2° C with 1 cm of precipitation (National Weather Service, 2023). The rainfall occurred at the end of the tracer injection and lasted for approximately one hour. The stream discharge prior to the tracer injection was 0.04 m<sup>3</sup>/s, with a stream width and depth of 2.8 m and 0.2 m, respectively. The injection started at 10:00 and continued for 4.3 h. The injection was kept at a constant rate of

approximately 0.8 L/min of dissolved NaCl (~222 mS/cm). A total of 45 kg of NaCl was injected into the stream. One hour of fluid conductivity background data was collected prior to the tracer injection and 20 hours of data were collected post injection. The fluid conductivity data collected 100m downstream from the injection point was particularly noisy so it was smoothed and filtered using a Hanning window width of nine. No other BTCs were smoothed. The ER data collection began on August 1 at 16:13, so there are 43 datasets or 18 hours of background data prior to the start of the injection. These datasets were averaged to produce one dataset representative of background conditions and to calculate background errors. The ER data collection continued during the injection and for a total of 24 hours after the injection was stopped. Data collection errors were quantified by at least three stacks for each measurement, and the stacking error averaged 0.1%. Inversion results produced a mean RMSE of 1.13% for all time steps. The RMSE is computed as the misfit between the data and the fitted model normalized by the noise.

### **2.4.3 September Tracer Test**

The average air temperature for the September 29, 2022 tracer test was 22.2° C with 0.02 cm of precipitation (National Weather Service, 2023). The measured stream discharge prior to the tracer injection was 0.03 m<sup>3</sup>/s, with a stream width and depth of 2.4 m and 0.2 m, respectively. The injection started at 09:31 and continued for 5 h with an injection rate of approximately 0.96 L/min of dissolved NaCl (~235 mS/cm). A total of 68 kg of NaCl were injected into the stream. Seventeen hours of fluid conductivity background data were collected prior to the tracer injection and 25 hours of data were collected post injection. The ER data collection began on September 28 at 15:47; the data collected between September 28 21:03 and September 29 09:05 were mistakenly over-written during data upload, so there are only 20 datasets or approximately 5.3 hours of background data prior to the start of the injection. The ER data collection continued

during injection and for a total of 25 hours after the injection was stopped. Data collection errors were quantified by at least three stacks for each measurement, and the stacking error averaged 0.1 %. Inversion results produced a mean RMSE of 1.07% for all time steps.

#### 2.4.4 Temporal Moments for Time-Series Analysis

Temporal moments of time-varying data have been used to compress time-series concentrations into useful statistics (Ward et al., 2014). These moments assume complete mixing of the tracer substance with water, negligible dispersion effects, and that the tracer mass will ultimately exit the aquifer system completely at one or more downgradient receptors as a function of time and discharge. Temporal moment analyses may be applied to the fluid EC and the bulk EC data. Previous work showed that the combined processes of advection and dispersion are dominantly responsible for shaping fluid BTCs prior to the time of peak tracer concentration, while transient storage processes are responsible for shaping the tails of experimental BTCs (Wagner & Harvey, 1997; Wagener et al., 2002; Scott et al., 2003; Wlostowski et al., 2013, 2017). Transient storage includes the hyporheic zone, in-stream eddies and pools, log jams, beaver dams, biofilms, and vegetation beds. As for bulk BTCs, past analyses (e.g., Singha & Gorelick, 2005) show that a low percentage of injected mass is seen in ER inversion models and ER inversion overparameterization leads to the inability and inaccuracy of mass estimation.

The fluid conductivity BTCs were used to perform the temporal moment analyses. The fluid and bulk conductivities were all temperature corrected and are reported as specific conductivity. The specific conductivity ( $\kappa_{25^{\circ}C}$ ) is calculated in accordance to U.S. Geological Survey (2019):

$$\kappa_{25^{\circ}C} = \frac{\kappa}{1 + \alpha(T - 25^{\circ}C)} \quad (2.1)$$

where  $\alpha$  is the temperature-compensation factor and  $T$  is the measured temperature in degrees Celsius. The  $n$ th order of a temporal moment ( $M_n$ ) is calculated in accordance with Keller and Frischknecht (1966):

$$M_n = \int_0^{\infty} t^n c(t) dt \quad (2.2)$$

$$c = \kappa_{25^\circ C} * 0.5 \quad (2.3)$$

where  $t$  is time in hours,  $n$  is the order of the moment, and  $c(t)$  is the observed concentration in mg/L as a function of time, which is calculated from the specific conductivity ( $\kappa_{(25^\circ C)}$ ). The zeroth moment ( $M_0$ ) multiplied by the discharge  $Q$  provides an estimate of the solute mass  $m$  to pass a measurement point:

$$m = M_0 * Q. \quad (2.4)$$

The first central moment ( $\mu_1$ ), once normalized to total concentration, is indicative of the mean arrival time ( $\bar{t}$ ) calculated using  $M_0$  and the first temporal moment ( $M_1$ ):

$$\mu_1 = \bar{t} = \frac{M_1}{M_0}. \quad (2.5)$$

This is the time it takes for 50% of the solute to arrive at a point. Subsequent temporal moments are defined about the centroid or first central moment. For example, the second central moment ( $\mu_2$ ) is calculated by:

$$\mu_2 = \sigma^2 = \frac{M_2}{M_0} - \left(\frac{M_1}{M_0}\right)^2. \quad (2.6)$$

The second central moment is interpreted as the variance of the concentration profile i.e., spreading. Finally, the third central moment ( $\mu_3$ ) describes the asymmetry of the BTC and is calculated with  $M_0$ ,  $M_1$ , the third temporal moment ( $M_3$ ), and  $\mu_2$ :

$$\mu_3 = \frac{M_3}{M_0} - 3\mu_2 \frac{M_1}{M_0} - \left(\frac{M_1}{M_0}\right)^3. \quad (2.7)$$

The third central moment can be interpreted as the skewness. Previous studies relate an increase in skewness with an increased transient storage (Harvey & Gorelick, 1995). A positive skewness

value indicates that the BTC is weighted to the right (has a heavy tail), recedes more gently than it rises, and suggests that the system is exhibiting some level of non-ideal behavior or that the transport of the solute is being influenced by factors beyond simple advection (Mull, 1988). Transient storage is caused by hyporheic exchange, turbulent flow in the open channel, and/or mixing with in-channel dead zones or channel side pockets (Ensign & Doyle, 2005; Wlostowski et al., 2017). The same method for BTC analyses with temporal moments was applied by Ward et al. (2010a) and Doughty et al. (2020) and a more detailed explanation may be found in their studies.

### **2.1.5 Results and Discussion**

Water levels, water temperature, fluid and bulk conductivity BTCs, temporal moments of those BTCs, and ER inversions were used to assess SW-GW connectivity, the hyporheic extent, and the implications for metal fate and transport. Results for each analysis are detailed below.

#### **2.5.1 Water Levels**

During the August and September tracer injection tests, the water levels in the study area exhibited differing local hydrologic conditions. The August test was performed when the stream was experiencing localized gaining conditions, based on GW elevations that were higher than SW elevations near the tracer injection site (Figure 2.3A). Conversely, the September test was conducted during localized losing conditions, where GW elevations were consistently below SW elevations (Figure 2.3B). However, we note that these conditions are local; the SW-GW gradients downstream of the injection site showed varying elevations at different locations along the stream (Figure A.1). Therefore, the localized measurements of SW-GW elevations near the injection site may not accurately represent the water levels of the entire stream or even the full reach of the injection. Rather, they reflect only the specific area of the measurements.

## 2.5.2 Temperature

Both SW and GW temperatures exhibit a recurring diel (24-hour) pattern (Figure 2.3B, 2.3D, and A.2). The GW and SW temperatures demonstrate an inverse relationship, with one increasing while the other decreases (Figure 2.3B and 2.3E). The SW temperature range observed in August (12-21 °C; Figure 3C) was greater than that observed in September (8-13 °C; Figure 2.3D). The SW temperatures during September fluctuate within a smaller temperature range due to the cooler outside air temperatures. Constant GW temperatures combined with variable SW temperatures indicate radiative forcing, as observed in the GW/SW temperatures during the September test (Figure 2.3F). Moreover, the temperatures recorded during the September tracer test show cooler temperatures during local losing conditions, indicating that losing conditions have minimal impact on temperature fluxes.

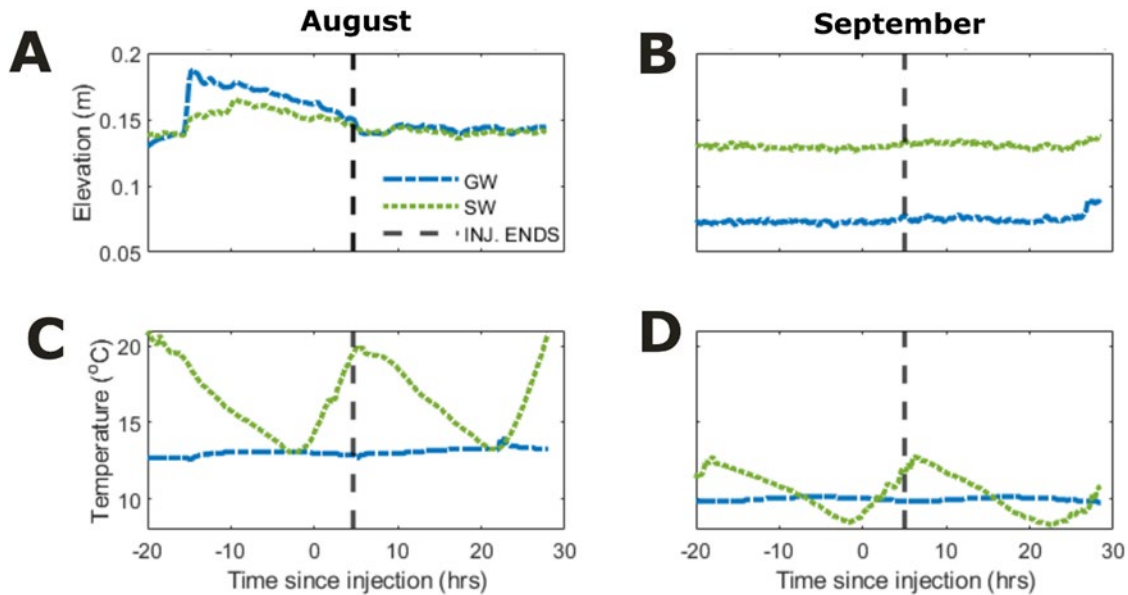


Figure 2.3: Data measured with a pressure transducer through time since injection start in wells upstream of the injection site, including the SW and GW elevations in A) August and B) September, and SW and GW temperatures in C) August and D) September.

### 2.5.3 Background Surface Water and Groundwater Specific Conductivity

Specific conductivity of surface water and groundwater can help in investigating hyporheic exchange, as it provides information about water sources, flowpaths, and exchange zones. As is often the case, the GW specific conductivity is consistently greater than the SW specific conductivity during the August (Figure 2.4A) and September (Figure 2.4B) tracer tests. In a gaining stream system, it is expected that there will be inputs to SW from the higher specific conductivity GW source. Following the completion of the August tracer injection, there is a notable increase in the specific conductivity of both SW and GW (Figure 2.4A). On the day of the tracer, there was an occurrence of afternoon rain towards the end of the injection period. This rainfall caused the previously clear-colored stream water to turn murky white. It is likely that this sharp rise in specific conductivity can be attributed to the rain event, which effectively flushed out sediments, colloids, and solutes from the shallow subsurface.

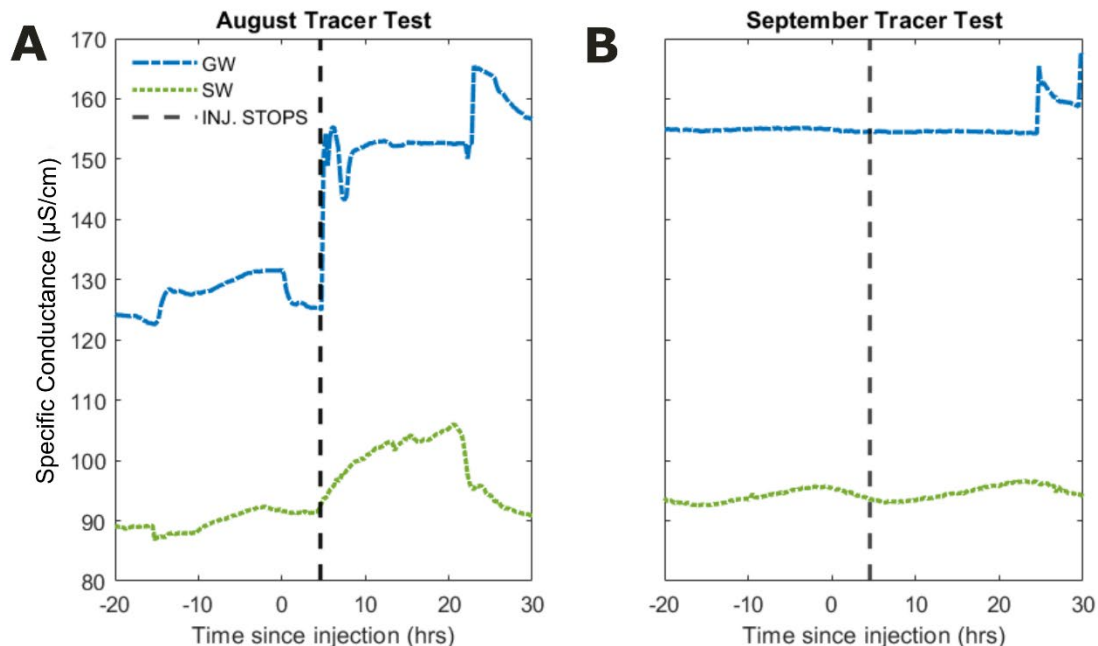


Figure 2.4: The SW and GW specific conductivity, as measured at the background loggers upstream of the injection point (Figure 2.1C) during the A) August and B) September tracer injection tests.

#### 2.5.4 Fluid and Bulk Conductivity Breakthrough Curves

The fluid and bulk specific conductivity BTCs (Figure 2.5) provide important insights into the advective and diffusive characteristics of the system. The background specific conductivity of the SW in August and September was ~85 and ~65 uS/cm, respectively, and increased to ~200 and ~235 uS/cm, respectively, during the tracer injection (Figure 2.5). Analysis of the fluid specific conductivity BTC at the transducer 100m downstream of the injection site during the September (Figure 2.5B) tracer test revealed a stable background prior to tracer injection. The background fluid specific conductivity prior to the injection during August was not recorded. The background bulk conductivity (Figure 2.5A) is higher in August when GW and SW temperatures were elevated relative to September. However, the bulk BTCs fluctuated during the background period, especially in August (Figure 2.5). Both bulk conductivity BTCs also showed an increase in conductivity after the tracer injection ended, approximately 12-27 hours after injection start (Figure 2.5). Notably, the bulk conductivity BTCs exhibited a diel cycle like that observed in the GW temperature data (Figure A.3), highlighting the known influence of temperature on bulk specific conductivity.

The fluid and bulk BTCs generally indicate that injecting enough tracer mass to significantly increase the concentration yields well-defined BTCs. While both the August and September bulk BTCs clearly show the tracer migration, the September test produced a cleaner signal. This may be due in part to the lower background bulk conductivity during the September tracer injection compared to the August injection. Since groundwater consistently had higher specific conductivity than stream water (Figure 2.4), we would—conceptually—expect gaining conditions to result in elevated stream specific conductivity. Instead, there is a dip in stream

specific conductivity following the start of the tracer test, which does not coincide with the expected conceptual behavior for a gaining stream.

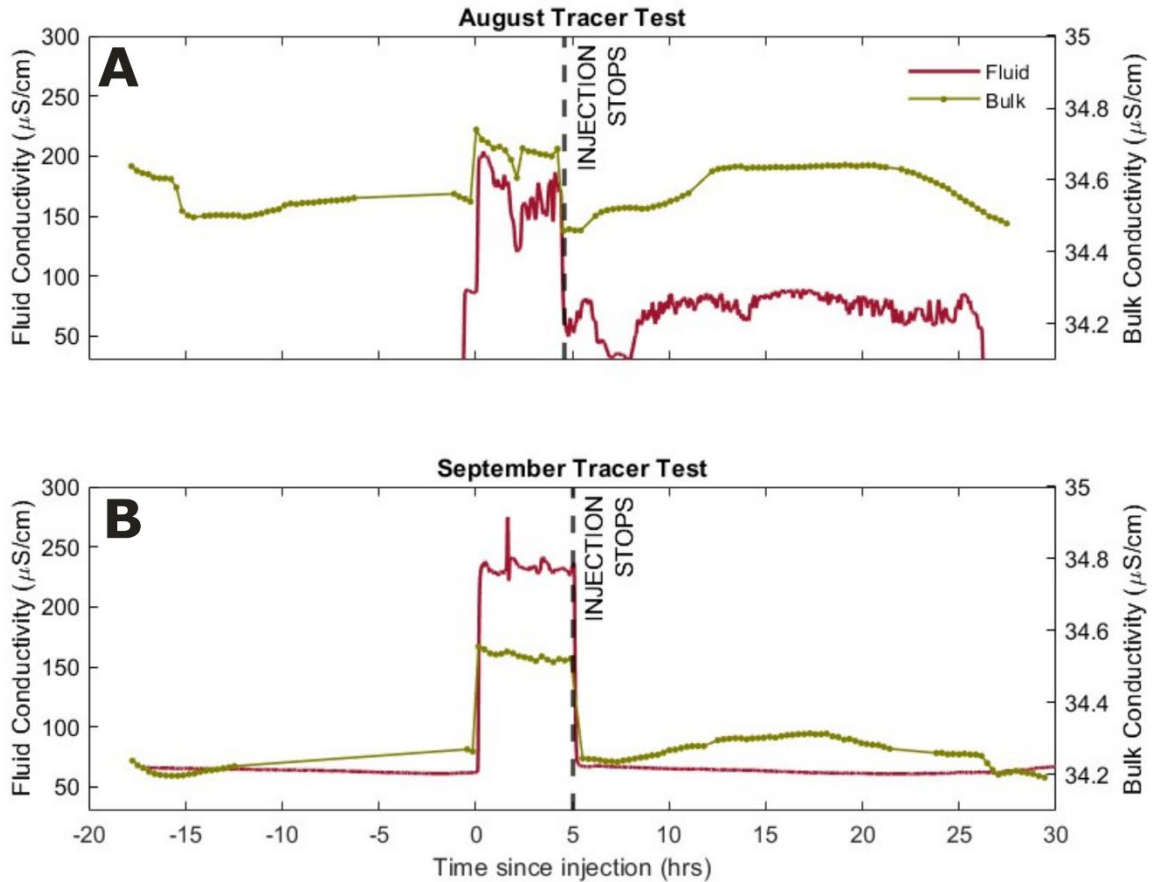


Figure 2.5: The non-normalized bulk conductivity and fluid conductivity measured 100 m downstream of the injection over time since injection during the A) August tracer test and the B) September tracer test.

### 2.5.5 Zeroth Temporal Moment: Solute Mass Breakthrough Curves

The results of the zeroth temporal moment analysis of the fluid specific conductivity BTCs describe the mass of recovered tracer downstream. Despite the nearly identical discharge for each tracer test ( $0.03 \text{ m}^3/\text{s}$  versus  $0.04 \text{ m}^3/\text{s}$ ) and qualitative similarities in the fluid specific conductivity BTCs, some important differences were noted. During the August test, the

transducer located 100m downstream, adjacent to the ER survey, showed concentration fluctuations, including a negative normalized concentration after background was removed (Figure 2.6A; Table 2.1). Additionally, the 250m downstream BTC showed a greater mass recovery (74%) than the 100m distance BTC (53%), which could be indicative of flowpaths moving under the 100m sensor or incomplete mixing. Meanwhile the 2300m BTC showed a mass recovery of 61%. This sensor is far enough downstream that it is impacted by eddies, pools, and vegetation, but it records a clear tracer signal: the same dip in fluid conductivity observed in the 100m and 250m BTCs 2 hr after injection starts is also observed in the 2300m downstream BTC approximately 7 hr after injection starts (Figure 2.6).

The BTC and ER data collected during September was similar to the August test data. Visual observation of the BTCs indicates the tracer was first observed within approximately 10 minutes of the injection start time at both the 100m and 250m locations and after 2.5 and 5.5 hours of the injection start time at the 1080m and 2300m downstream locations, respectively (Figure 2.6B). The recorded tracer mass at the estimated mixing zone (100m downstream) was approximately 92% of the total injected mass, and this percentage decreased at the other locations: the recorded tracer mass 250m, 1080m, and 2300m downstream were 86%, 88%, and 70%, respectively (Figure 2.6B; Table 2.1). There was minimal tailing visually noted at the 100m downstream location, but tailing became more apparent at other downstream locations, presumably as mass was retained in surface and subsurface transient storage zones along the tracer flowpaths. The time of tracer movement often exceeds the time of data collection (or the “window of detection”), meaning the complete recovery of the tracer may not be recorded. This issue is particularly problematic because the measurement points further downstream; 1080m and 2300m produce the lowest mass recoveries, perhaps for this reason. In general, a discharge of

0.04 m<sup>3</sup>/s and gaining stream conditions resulted in lower percentages of mass recovery than a discharge of 0.03 m<sup>3</sup>/s and losing stream conditions (Table 2.1). We would expect a net gaining stream to have higher mass recovery rates, but this does not coincide with the observed BTCs' behavior (Figure 2.6). A plausible explanation, which underlies several uncertainties, is that the low stream conductivity combined with the higher background bulk conductivity and low solute mass injection led to a less-than-successful tracer injection for the August tracer test during gaining stream conditions.

These results may be summarized by several key findings. There was no clear trend observed between percent mass recovery and distance downstream of the injection (Figure 2.6). Additionally, the minimal tailing in the upstream locations i.e., 100m and 250m, indicate there is minimal subsurface retention. Further downstream BTCs i.e., 1080m and 2300m, show an increased but still minimal tailing, likely because of additional in-stream transient storage; it is not uncommon to have fallen trees and beaver dams in this area, which may increase the instream transient storage and overall solute retention.

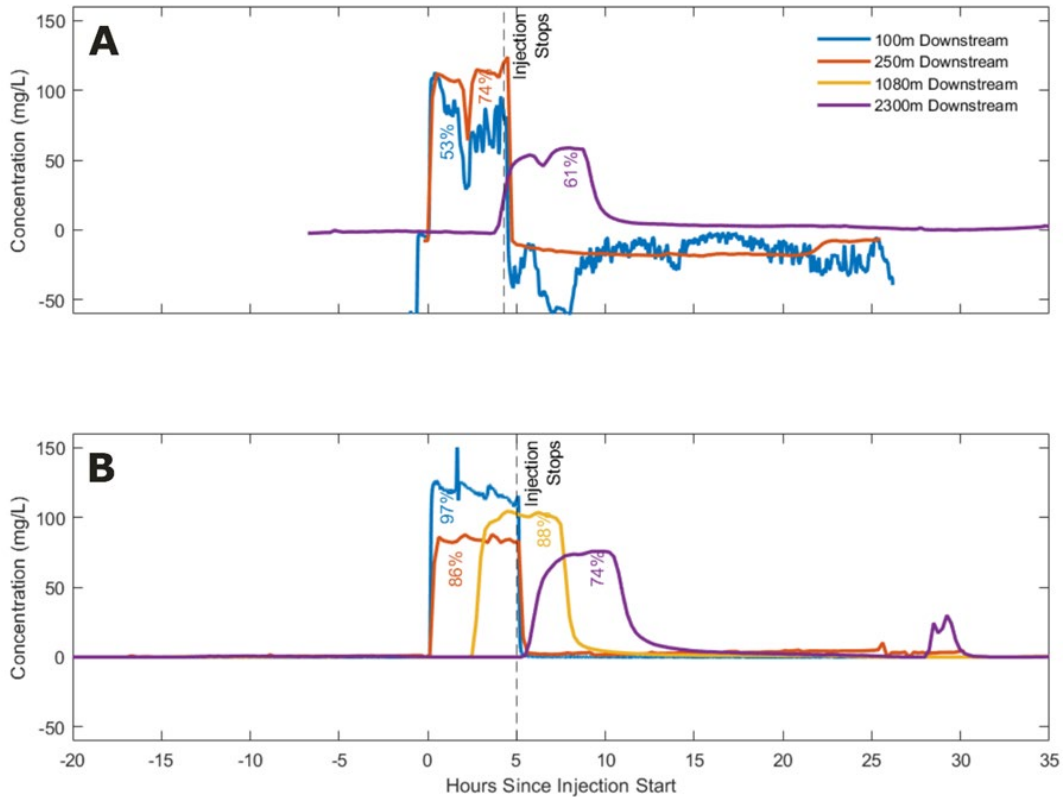


Figure 2.6: Surface water BTCs measured at A) 100m, 250m, and 2300m downstream from the injection site during the August tracer experiment and B) 100m, 250m, 1080m, and 2300m downstream from the injection site during the September tracer experiments, with percent of mass recovery shown within each curve. The mass injected was 45 kg for August and 68 kg for September. The BTCs are shown as NaCl concentrations (as calculated from the specific conductivity). Note issues during the August test at the 100 m location, where the background-adjusted concentration reached negative values, possibly because the sensor was not fully submerged for the entirety of the tracer test.

<b>Fluid Mass Recovered</b>				
<b>Downstream Location</b>	<b><u>August</u></b>		<b><u>September</u></b>	
100m	24 kg	53%	66 kg	96%
250m	33 kg	74%	59 kg	86%
1080m	NC	-----	60 kg	88%
2300m	28 kg	61%	33 kg	74%
Total Mass injected:	45 kg	100%	68 kg	100%

Table 2.1: The recovered mass in kilograms and as a percentage in the stream as calculated for each downstream location using the zeroth moment. The total mass of tracer injected for each tracer test is also shown. The mass injected was 45 kg for August and 68 kg for September. NC indicates data was not collected.

### 2.5.6 Inversion of Resistivity Data

The ER inversions show the spatial and temporal dynamics of tracer migration, highlighting the extent of the hyporheic zone under baseflow conditions in August and September. In the August test, the background ER model (Figure 2.7A) shows a highly resistive (i.e., low conductivity) stream ( $X=5-8\text{m}$ ) and floodplain ( $X=18-25\text{m}$ ). Upon injection, the ER inversion models reveal a conductivity increase in the stream, streambed, and streambanks ( $X=5-8$  and  $Y=0-3$ ; Figure 2.7C-H), with a maximum increase in conductivity of 35% from background conditions. The tracer is observed to a maximum depth of approximately 2.5m below the water surface. The tracer is more quickly flushed out of the stream, streambed, and streambank than from the floodplain, which experiences a subtle conductivity increase of approximately 8% at  $X=15-25\text{m}$  within the top 1m below the ground surface (Figure 2.7C-H). The tracer is flushed out of the system 4 hours after injection stops.

The September ER inversions display a similarly resistive stream ( $X=5-8\text{m}$ ) and floodplain ( $X=18-25\text{m}$ ). The tracer is concentrated at the stream, stream banks, and the streambed

to a maximum depth of approximately 2 m (Figure 2.8C-H). There is no tracer observed at the floodplain ( $X=15-24\text{m}$ ; Figure 2.8C-H). Some areas in the September inversion models between  $X=10-30$  and a depth of 1-5m appear to show changes in conductivity from the background; however, these areas are either outside of the depth of investigation (DOI) or have low resolution (Figure 2.8B). The September ER inversions represent the tracer restricted to the shallow subsurface below the streambed and the streambanks (Figure 2.8).

The hyporheic extent during the August experiment (discharge of  $0.04\text{ m}^3/\text{s}$  and gaining stream) appears to be only slightly more extensive than in September (discharge of  $0.03\text{ m}^3/\text{s}$  and losing stream), based on the relative sizes of the tracer mapped in the ER inversion models (Figures 2.7C-H, 2.8C-H). The hyporheic extent appears horizontally wide in August. The similarity between both experiments can be explained by the nearly identical discharges between both experiments; discharge is usually a control on hyporheic area. Interestingly, the flow regime (i.e., gaining versus losing) was not a greater contributor to the hyporheic extent. There is not a notable difference between the SW and GW elevations during the August tracer test (Figure 2.3A), meaning that they might fluctuate and change direction from gaining to losing easily. This potential for fluctuation between SW and GW conditions might lead one to think that a higher exchange is created between the two water sources in the hyporheic zone. In contrast, the SW and GW elevations during the September test show notably different elevations, with the SW elevation being nearly double that of the GW elevation (Figure 2.3B), indicating strong losing conditions. These water level differences might explain the slight difference in the hyporheic extents between both tracer experiments.

Further analysis of water elevations at two downstream locations (1080m and 2300m; Figure A.1) reveal differences in flow regime patterns between the data collected near the

injection site (Figure 2.3A, B) and the two downstream locations (Figure A.1). The upstream location, near the injection site exhibited locally gaining conditions, but September experienced losing conditions. However, the stream consistently exhibited gaining behavior 1080m downstream during both August and September (Figure A.1B, E), and it consistently exhibited losing behavior 2300m downstream during both months (Figure A.1C, F). The SW and GW elevations at the injection area fluctuate between losing and gaining conditions and can be considered near-neutral since their elevations are not far apart. The near-neutrality can allow a higher potential of hyporheic exchange. The two downstream locations do not seem to fluctuate and therefore likely experience a lower potential for hyporheic exchange. Previous studies show that increasing net gain or loss magnitudes relative to a neutral stream exponentially decrease hyporheic exchange and hyporheic area (Cardenas, 2009; Fox et al., 2016; Trauth et al., 2013). As a result, a larger hyporheic extent and increased mixing between SW and GW would be expected at the injection site and specifically during the August tracer test, but the hyporheic extent during August was not notably greater than that seen in September.

The background ER surveys (Figures 2.7A, 3.7A) indicate that the stream and floodplain have similarly low ECs during both tracer tests, suggesting a possible connection between the stream and floodplain. This result is supported by the gaining stream conditions present during the August tracer test. But during the September tracer test, the stream is locally losing, and we also see an overall lower background in bulk EC. Because the subsurface has a lower bulk EC than the stream, the salt tracer is likely not migrating into the subsurface during the September test. Additionally, the floodplain and stream may be resistive due to rainfall and morning dew, which occur frequently during the warmer months in Crested Butte. These similar ER inversion models between both tracer tests given different flow regimes may indicate that the discharge is the main

hyporheic extent driver even in this stream system. Overall, the ER inversions provide qualitative information on the spatial and temporal behavior of the tracer, indicating where the tracer traveled and the extent of the hyporheic zone during baseflow conditions.

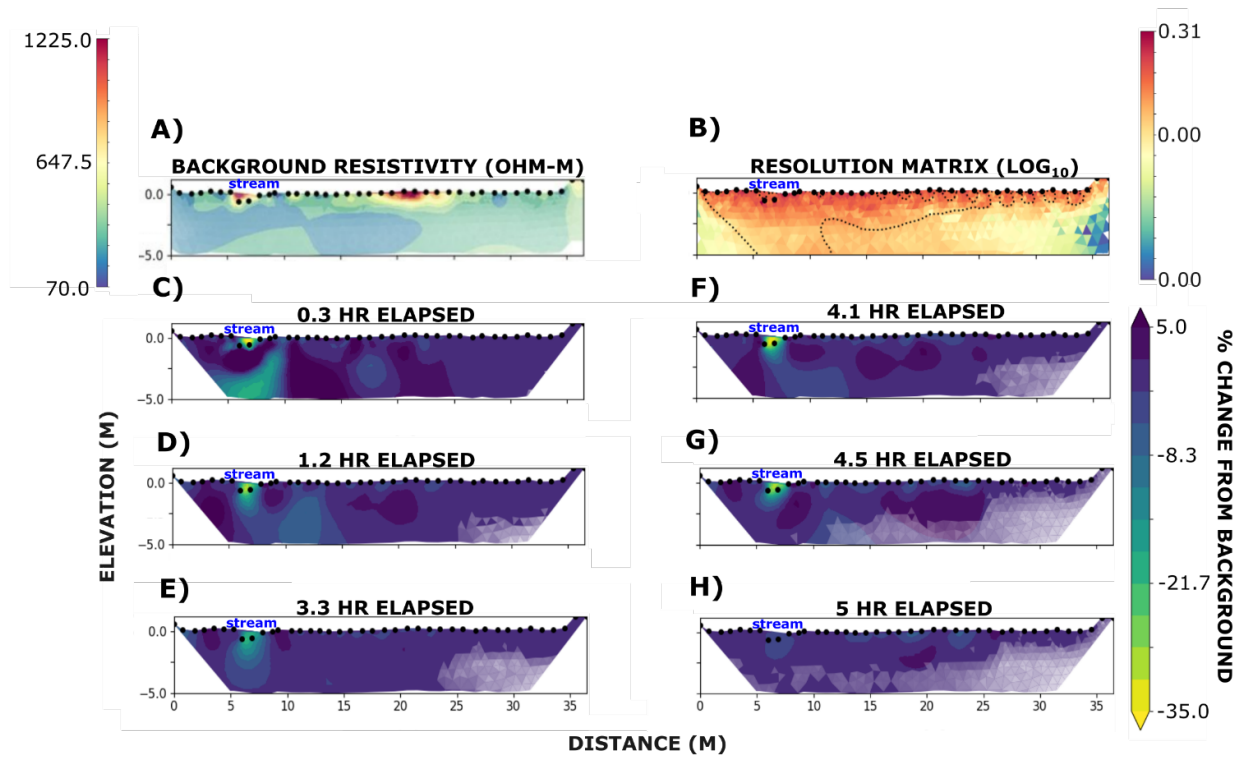


Figure 2.7: Cross-sectional ER inversions from August, with stream flow directed out of the page. A) The pre-injection electrical resistivity model with distance (m) in the x-axis and elevation on the y-axis (m). Areas of high resistivity (the cobble-bed stream at X=5-8 m and the floodplain at X=18-25 m) are likely preferred flowpaths, based on changes in ER shown below. B) The diagonal of the resolution matrix, which measures how well the model parameters are resolved by the data, i.e., a value close to 1 would indicate perfect model resolution from data. The dashed line is the depth of investigation (DOI). C–H) Selected ER inversions for the tracer injection test (see Appendix B for all images) as percent changes from the pre-injection electrical resistivity model at time elapsed from the start of tracer injection.

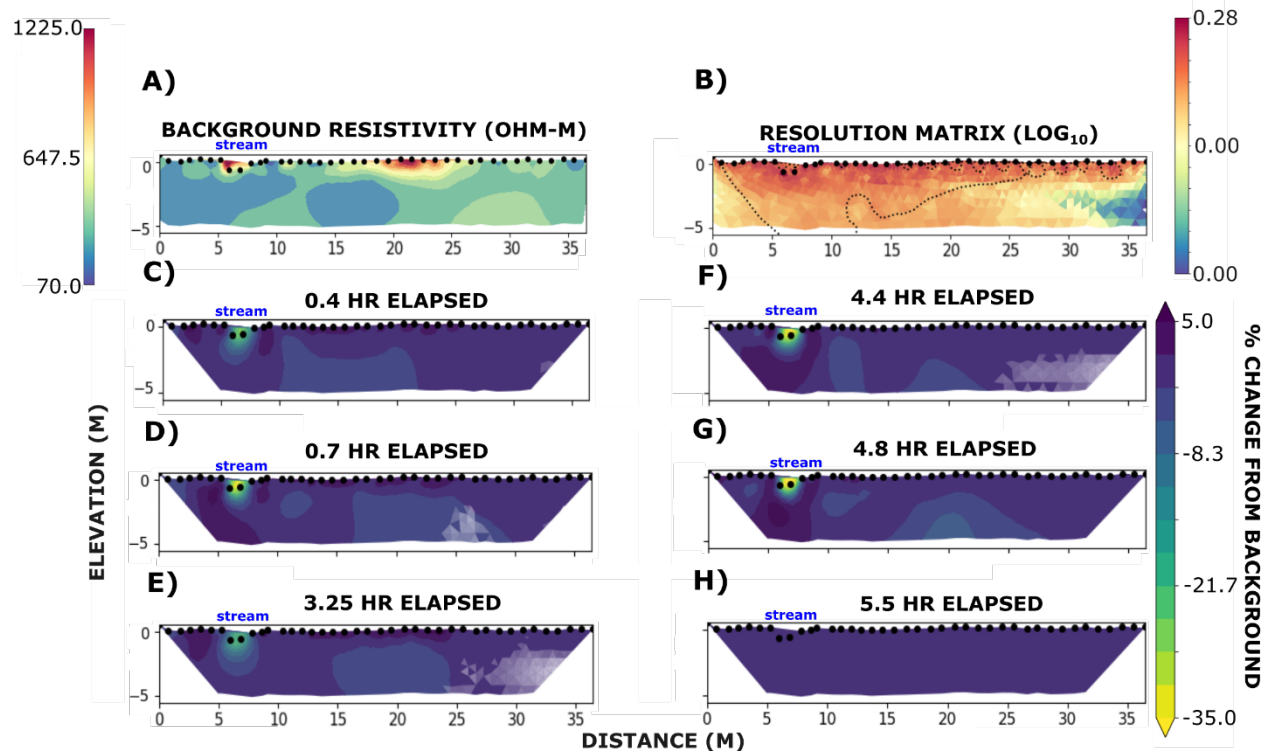


Figure 2.8: Inversion models from September are presented as cross-sections transverse to the stream with stream flow directed out of the page. A) The pre-injection electrical resistivity model with distance (m) in the x-axis and elevation on the y-axis (m). B) The diagonal of the true resolution matrix, which measures how well the data and the model parameters are resolved i.e., any resolution value close to 1 would indicate equal predicted and measured values. The dashed line is the depth of investigation (DOI). C–H) Selected ER inversions for the tracer injection test (see Appendix B for all images) as percent changes from the pre-injection electrical resistivity model at time elapsed after beginning the conservative solute injection. C–G) Decrease in bulk resistivity in the subsurface due to tracer presence. H) The tracer is flushed from the subsurface.

The limited SW-GW interactions and hyporheic area found in these data may be a result of several physical contributors. First, the maximum depth to bedrock near Coal Creek is approximately 15 m, but in several areas the Mt. Axell laccolith bedrock surfaces to the stream level (Gaskill et al., 1987), which would impede solutes and groundwater to travel to depth. Also, during shallow soil augering activities for soil sampling adjacent to the stream, we noted that there is clay at approximately 30 cm below the ground surface. Clay has low permeability and limits SW-GW exchange. Additionally, biofilms are common in alpine streams where they are

prolific and highly active at the streambed (Battin et al., 2016), and environmental conditions are most favorable for promoting the growth of biofilms during low discharge and during lower snowmelt (Battin et al., 2004). Microbial biofilms can also act as barriers for SW-GW exchange by reducing hydraulic conductivity of sediments and therefore limit water penetration and solute transfer within the hyporheic zone (Aubeneau et al., 2016) and are likely a factor here, although unmeasured.

### **2.5.7 Implications of Results**

The goal of this study was to explore the hyporheic extent and constrain the influence it may have on metal fate and transport in the Coal Creek watershed. With such minimal differences in the hyporheic zone extents between tracer tests under a 0.04 m<sup>3</sup>/s discharge and gaining stream conditions and under a 0.03 m<sup>3</sup>/s discharge and losing stream conditions the potential for metals to be exchanged between SW and GW appears similar for both conditions observed. This means many of the ecosystem services provided by the hyporheic zone such as metal precipitation, oxidation, adsorption or other biogeochemical transformations, are unlikely to be prevalent here. For many metals, biogeochemical transformation in the hyporheic zone can reduce metal mobility and toxicity (Borch et al., 2010; DeVore et al., 2022), and the hyporheic zone may act as a sink for metals, buffering water quality. Instead, in this system, metals released to the stream are expected to be transported downstream with minimal interaction between the stream and hyporheic zone (i.e., advection-dominated flow). The naturally occurring heavy metals in the area will be flushed downstream to reach the treatment plant and/or the downstream town of Crested Butte.

## 2.6 Conclusions

Even though the gaining and losing conditions were determined only at three locations in a reach of three km with discrete measurements, these localized stream conditions can still have an impact on hyporheic exchange. During the August tracer test, which was performed during a  $0.04 \text{ m}^3/\text{s}$  discharge and localized gaining stream conditions, the hyporheic zone extended to  $\sim 2.5$  m below the streambed and slightly into the streambanks and into the floodplain adjacent to the stream. In contrast, during the September tracer test, which was performed during a  $0.03 \text{ m}^3/\text{s}$  discharge and localized losing stream conditions, the hyporheic zone was constrained to  $\sim 2$  m below the streambed and the immediate banks. During gaining stream conditions (August) the stream and floodplain exhibited similar conductivities, but this changed during localized losing conditions (September) where the stream water and floodplain did not have similar conductivities, implying more disconnection in the later test.

The BTCs from the tracer tests showed minimal skewness and thus retention, and the data collection window was likely not long enough to reach full tracer mass recovery, especially at measurement locations further downstream. The fluid mass recovery reveals that there is overall lower mass recovery during the time of data collection during losing stream conditions, as might be expected (Table 2.1).

In general, the hyporheic area of this system appears to be similarly limited under both gaining and losing conditions. The vertical depth of the hyporheic zone and connection to a surrounding floodplain were greater during August (gaining conditions), but there was minimal tailing and limited exchange under both conditions. Consequently, there is a low capacity for the hyporheic zone to do biogeochemical work, and little ability to buffer or sequester metal loads from metal-laden bedrock and abandoned mines in the watershed. Overall, this study suggests that

the hyporheic zone has a limited role in maintaining the health and productivity of this river ecosystem, at least at baseflow conditions.

## CHAPTER 3

### FUTURE WORK

Here, I outline some ideas that would have helped make this work more complete and successful.

#### **3.1 Tracer tests at higher discharge**

This study was constrained to baseflow conditions because the electrical resistivity (ER) data collected during higher discharge flows were collected with gap fillers, which produced unequal sequences and therefore made the screening of data for inversion too time consuming. Future studies would benefit from performing the tracer during high and medium flow conditions at the same location, using the same arrays. Doing so could allow for more reliable correlations in the time-variable statistics calculated from temporal moments. Additionally, it would allow us to test the impact discharge has on the extent of the hyporheic zone.

#### **3.2 Tracer mass**

A greater tracer mass should be injected into the stream during the tracer tests. The 45 kg of tracer used in August did not provide a large enough concentration change from the background conditions, especially for bulk conductivity. The 65 kg tracer mass used in September provided a greater increase from both the fluid and bulk background levels. This increase from the background specific conductivity—both fluid and bulk—is expected to perform even better during higher discharge flows.

#### **3.3 Equipment**

A precise low-flow meter should be used to prevent injection flow fluctuations like those observed during what should be a plateau in the August breakthrough curves (BTCs) from manual

handling of flow rate. There were many abrupt solute mass concentrations decreases observed specifically in the BTCs and these would be avoided if a more precise flowmeter had been used and preset without having to modify during the duration of the test.

### **3.4 Data collection**

There were inconsistencies with the length of background data that was collected. Therefore, a longer background collection period during the same conditions as tracer injection test should have been collected for both ER and electrical conductivity (EC). At least 24 hours prior and post tracer injection should be collected.

### **3.5 Geochemistry Sampling**

To more accurately assess any impact or role the hyporheic zone plays on metal fate and transport, groundwater (GW) and surface water (SW) geochemistry samples including major cations, major anions, alkalinity, and metal(loid)s should be collected and analyzed at the different locations (injection site, 100m, 250m, 1080m, and 2300m). These data could lead to better understanding how water quality and metal(loid) loading varies with changing stream flow, changing flow regime (i.e., losing or gaining), and changing hyporheic extent and hyporheic flow.

### **3.6 Gaining and Losing Stream Measurements**

Several studies have already explored the effects of SW-GW net fluxes and its effect on hyporheic exchange and the hyporheic extent. A well-structured analysis of the flow regime in the study area could help better explain the net fluxes between SW-GW on hyporheic extent and hyporheic flow in this system. A field measurement plan for stream slug-tracer experiments, like those outlined in Payn et al., (2009) could have been used to elucidate to locations where gaining and losing conditions are present along the stream and thus where hyporheic flowpaths are likely to be present and have potential for biogeochemical work.

### **3.7 Fiber Optic Distributed Temperature Sensing**

A fiber optic distributed temperature sensing (FO-DTS) cable could also be employed during the tracer tests at the study locations (injection site, 100m, 250m, 1080m, and 2300m) to measure temperature anomalies in the stream and map gaining conditions where GW contributes to the stream.

### **3.8 Coupled Modeling**

The assessment of metal fate and transport in the study reach can be modeled with software such as One-Dimensional Transport with Inflow and Storage (OTIS), developed by the U.S. Geological Survey (USGS) for streams and rivers. Additionally, MODFLOW and/or MT3D may also be used to explore different physical components, such as logjams and beaver dams, affecting hyporheic exchange (e.g., Doughty et al., 2020). Given a model, we could explore how differences in flow regimes, clay and bedrock, logjams/beaver dams, discharge, etc. affect hyporheic exchange.

## REFERENCES

- Aubeneau, A. F., Hanrahan, B., Bolster, D., & Tank, J. (2016). Biofilm growth in gravel bed streams controls solute residence time distributions. *Journal of Geophysical Research: Biogeosciences*, *121*(7), 1840–1850. <https://doi.org/10.1002/2016JG003333>
- Battin, T. J., Besemer, K., Bengtsson, M. M., Romani, A. M., & Packmann, A. I. (2016). The ecology and biogeochemistry of stream biofilms. *Nature Reviews. Microbiology*, *14*(4), 251–263. <https://doi.org/10.1038/nrmicro.2016.15>
- Battin, T. J., Wille, A., Psenner, R., & Richter, A. (2004). Large-scale environmental controls on microbial biofilms in high-alpine streams. *Biogeosciences*, *1*(2), 159–171. <https://doi.org/10.5194/bg-1-159-2004>
- Benner, S. G., Smart, E. W., & Moore, J. N. (1995). Metal Behavior during Surface-Groundwater Interaction, Silver Bow Creek, Montana. *Environmental Science & Technology*, *29*(7), 1789–1795. <https://doi.org/10.1021/es00007a015>
- Blanchy, G., Saneiyani, S., Boyd, J., McLachlan, P., & Binley, A. (2020). ResIPy, an intuitive open source software for complex geoelectrical inversion/modeling. *Computers & Geosciences*, *137*, 104423. <https://doi.org/10.1016/j.cageo.2020.104423>
- Boano, F., Demaria, A., Revelli, R., & Ridolfi, L. (2010). Biogeochemical zonation due to intrameander hyporheic flow. *Water Resources Research*, *46*(2). <https://doi.org/10.1029/2008WR007583>
- Boano, F., Revelli, R., & Ridolfi, L. (2008). Reduction of the hyporheic zone volume due to the stream-aquifer interaction. *Geophysical Research Letters*, *35*(9). <https://doi.org/10.1029/2008GL033554>
- Borch, T., Kretzschmar, R., Kappler, A., Cappellen, P. V., Ginder-Vogel, M., Voegelin, A., & Campbell, K. (2010). Biogeochemical Redox Processes and their Impact on Contaminant Dynamics. *Environmental Science & Technology*, *44*(1), 15–23. <https://doi.org/10.1021/es9026248>
- Boulton, A. J., Findlay, S., Marmonier, P., Stanley, E. H., & Valett, H. M. (1998). The Functional Significance of the Hyporheic Zone in Streams and Rivers. *Annual Review of Ecology and Systematics*, *29*(1), 59–81. <https://doi.org/10.1146/annurev.ecolsys.29.1.59>
- Briggs, M. A., Day-Lewis, F. D., Ong, J. B., Harvey, J. W., & Lane, J. W. (2014). Dual-domain mass-transfer parameters from electrical hysteresis: Theory and analytical approach applied to laboratory, synthetic streambed, and groundwater experiments. *Water Resources Research*, *50*(10), 8281–8299. <https://doi.org/10.1002/2014WR015880>
- Brown, L. E., Hannah, D. M., & Milner, A. M. (2006). Hydroclimatological influences on water column and streambed thermal dynamics in an alpine river system. *Journal of Hydrology*, *325*(1), 1–20. <https://doi.org/10.1016/j.jhydrol.2005.09.025>

- Cardenas, M. B. (2009). Stream-aquifer interactions and hyporheic exchange in gaining and losing sinuous streams. *Water Resources Research*, 45(6).  
<https://doi.org/10.1029/2008WR007651>
- Cardenas, M. B. (2015). Hyporheic zone hydrologic science: A historical account of its emergence and a prospectus. *Water Resources Research*, 51(5), 3601–3616.  
<https://doi.org/10.1002/2015WR017028>
- Clements, W. H., Carlisle, D. M., Lazorchak, J. M., & Johnson, P. C. (2000). Heavy Metals Structure Benthic Communities in Colorado Mountain Streams. *Ecological Applications*, 10(2), 626–638. [https://doi.org/10.1890/1051-0761\(2000\)010\[0626:HMSBCI\]2.0.CO;2](https://doi.org/10.1890/1051-0761(2000)010[0626:HMSBCI]2.0.CO;2)
- Cochand, M., Christe, P., Ornstein, P., & Hunkeler, D. (2019). Groundwater Storage in High Alpine Catchments and Its Contribution to Streamflow. *Water Resources Research*, 55(4), 2613–2630. <https://doi.org/10.1029/2018WR022989>
- Coppola, E., Raffaele, F., & Giorgi, F. (2018). Impact of climate change on snow melt driven runoff timing over the Alpine region. *Climate Dynamics*, 51(3), 1259–1273.  
<https://doi.org/10.1007/s00382-016-3331-0>
- DeGraff, J. V. (2007). Addressing the toxic legacy of abandoned mines on public land in the western United States. In J. V. DeGraff (Ed.), *Understanding and Responding to Hazardous Substances at Mine Sites in the Western United States* (Vol. 17, p. 0). Geological Society of America. [https://doi.org/10.1130/2007.4017\(01\)](https://doi.org/10.1130/2007.4017(01))
- Dennehy, K. F., Litke, D. W., Tate, C. M., & Heiny, J. S. (1993). South Platte River Basin—Colorado, Nebraska, and Wyoming1. *JAWRA Journal of the American Water Resources Association*, 29(4), 647–683. <https://doi.org/10.1111/j.1752-1688.1993.tb03231.x>
- DeVore, C. L., Rodriguez-Freire, L., Villa, N., Soleimanifar, M., Gonzalez-Estrella, J., Ali, A. M. S., Lezama-Pacheco, J., Ducheneaux, C., & Cerrato, J. M. (2022). Mobilization of As, Fe, and Mn from Contaminated Sediment in Aerobic and Anaerobic Conditions: Chemical or Microbiological Triggers? *ACS Earth and Space Chemistry*, 6(7), 1644–1654.  
<https://doi.org/10.1021/acsearthspacechem.1c00370>
- Doetsch, J., Linde, N., Vogt, T., Binley, A., & Green, A. G. (2012). Imaging and quantifying salt-tracer transport in a riparian groundwater system by means of 3D ERT monitoring. *Geophysics*, 77(5), B207–B218. <https://doi.org/10.1190/geo2012-0046.1>
- Doughty, M., Sawyer, A. H., Wohl, E., & Singha, K. (2020). Mapping increases in hyporheic exchange from channel-spanning logjams. *Journal of Hydrology*, 587, 124931.  
<https://doi.org/10.1016/j.jhydrol.2020.124931>
- Ensign, S. H., & Doyle, M. W. (2005). In-channel transient storage and associated nutrient retention: Evidence from experimental manipulations. *Limnology and Oceanography*, 50(6), 1740–1751. <https://doi.org/10.4319/lo.2005.50.6.1740>

- Fields, J. F., & Dethier, D. P. (2019). From on high: Geochemistry of alpine springs, Niwot Ridge, Colorado Front Range, USA. *Hydrological Processes*, 33(12), 1756–1774. <https://doi.org/10.1002/hyp.13436>
- Fischer, H., Kloep, F., Wilzcek, S., & Pusch, M. (2005). A River's Liver – Microbial Processes within the Hyporheic Zone of a Large Lowland River. *Biogeochemistry*, 76, 349–371. <https://doi.org/10.1007/s10533-005-6896-y>
- Fox, A., Laube, G., Schmidt, C., Fleckenstein, J. H., & Arnon, S. (2016). The effect of losing and gaining flow conditions on hyporheic exchange in heterogeneous streambeds. *Water Resources Research*, 52(9), 7460–7477. <https://doi.org/10.1002/2016WR018677>
- Fuller, C. C., & Harvey, J. W. (2000). Reactive Uptake of Trace Metals in the Hyporheic Zone of a Mining-Contaminated Stream, Pinal Creek, Arizona. *Environmental Science & Technology*, 34(7), 1150–1155. <https://doi.org/10.1021/es990714d>
- Gandy, C. J., Smith, J. W. N., & Jarvis, A. P. (2007). Attenuation of mining-derived pollutants in the hyporheic zone: A review. *Science of The Total Environment*, 373(2), 435–446. <https://doi.org/10.1016/j.scitotenv.2006.11.004>
- Gaona, J., Meinikmann, K., & Lewandowski, J. (2019). Identification of groundwater exfiltration, interflow discharge, and hyporheic exchange flows by fibre optic distributed temperature sensing supported by electromagnetic induction geophysics. *Hydrological Processes*, 33(10), 1390–1402. <https://doi.org/10.1002/hyp.13408>
- Gaskill, D., DeLong, J., & Cochran, D. (1987). *Geologic map of the Mt. Axtell quadrangle, Gunnison County, Colorado*. USGS. <https://doi.org/10.3133/gq1604>
- González-Pinzón, R., Dorley, J., Singley, J., Singha, K., Gooseff, M., & Covino, T. (2022). TIPT: The Tracer Injection Planning Tool. *Environmental Modelling & Software*, 156, 105504. <https://doi.org/10.1016/j.envsoft.2022.105504>
- Gooseff, M. N., Payn, R. A., Zarnetske, J. P., Bowden, W. B., McNamara, J. P., & Bradford, J. H. (2008). Comparison of in-channel mobile–immobile zone exchange during instantaneous and constant rate stream tracer additions: Implications for design and interpretation of non-conservative tracer experiments. *Journal of Hydrology*, 357(1), 112–124. <https://doi.org/10.1016/j.jhydrol.2008.05.006>
- Harvey, C. F., & Gorelick, S. M. (1995). Temporal Moment-Generating Equations: Modeling Transport and Mass Transfer in Heterogeneous Aquifers. *Water Resources Research*, 31(8), 1895–1911. <https://doi.org/10.1029/95WR01231>
- Heil, E., Warix, S., Singha, K., & Navarre-Sitchler, A. (2022). Decadal trends in solute concentrations, mass flux, and discharge reveal variable hydrologic and geochemical response to climate change in two alpine watersheds. *Applied Geochemistry*, 144, 105402. <https://doi.org/10.1016/j.apgeochem.2022.105402>

- Hoagland, B., Navarre-Sitchler, A., Cowie, R., & Singha, K. (2020). Groundwater–Stream Connectivity Mediates Metal(loid) Geochemistry in the Hyporheic Zone of Streams Impacted by Historic Mining and Acid Rock Drainage. *Frontiers in Water*, 2. <https://www.frontiersin.org/articles/10.3389/frwa.2020.600409>
- Hood, J. L., & Hayashi, M. (2015). Characterization of snowmelt flux and groundwater storage in an alpine headwater basin. *Journal of Hydrology*, 521, 482–497. <https://doi.org/10.1016/j.jhydrol.2014.12.041>
- Hrozencik, R. A. (2021). Trends in U.S. Irrigated Agriculture: Increasing Resilience Under Water Supply Scarcity. *SSRN Electronic Journal*. <https://doi.org/10.2139/ssrn.3996325>
- Kerndorff, H., & Schnitzer, M. (1980). Sorption of metals on humic acid. *Geochimica et Cosmochimica Acta*, 44(11), 1701–1708. [https://doi.org/10.1016/0016-7037\(80\)90221-5](https://doi.org/10.1016/0016-7037(80)90221-5)
- Lee, G., Bigham, J. M., & Faure, G. (2002). Removal of trace metals by coprecipitation with Fe, Al and Mn from natural waters contaminated with acid mine drainage in the Ducktown Mining District, Tennessee. *Applied Geochemistry*, 17(5), 569–581. [https://doi.org/10.1016/S0883-2927\(01\)00125-1](https://doi.org/10.1016/S0883-2927(01)00125-1)
- Lewandowski, J., Arnon, S., Banks, E., Batelaan, O., Betterle, A., Broecker, T., Coll, C., Drummond, J. D., Gaona Garcia, J., Galloway, J., Gomez-Velez, J., Grabowski, R. C., Herzog, S. P., Hinkelmann, R., Höhne, A., Hollender, J., Horn, M. A., Jaeger, A., Krause, S., ... Wu, L. (2019). Is the Hyporheic Zone Relevant beyond the Scientific Community? *Water*, 11(11), Article 11. <https://doi.org/10.3390/w11112230>
- Magliozzi, C., Grabowski, R. C., Packman, A. I., & Krause, S. (2018). Toward a conceptual framework of hyporheic exchange across spatial scales. *Hydrology and Earth System Sciences*, 22(12), 6163–6185. <https://doi.org/10.5194/hess-22-6163-2018>
- McCabe, G. J., & Clark, M. P. (2005). Trends and Variability in Snowmelt Runoff in the Western United States. *Journal of Hydrometeorology*, 6(4), 476–482. <https://doi.org/10.1175/JHM428.1>
- Niyogi, D. K., Lewis, Jr., William M., & McKnight, D. M. (2002). Effects of Stress from Mine Drainage on Diversity, Biomass, and Function of Primary Producers in Mountain Streams. *Ecosystems*, 5(6), 554–567. <https://doi.org/10.1007/s10021-002-0182-9>
- Rauscher, S. A., Pal, J. S., Diffenbaugh, N. S., & Benedetti, M. M. (2008). Future changes in snowmelt-driven runoff timing over the western US. *Geophysical Research Letters*, 35(16). <https://doi.org/10.1029/2008GL034424>
- Ryan, J. N., & Bevan, H. (2009). *Sources of Metal Contamination in the Coal Creek Watershed, Crested Butte, Gunnison County, Colorado: Part II. High Flow, June 2006.*
- Ryan, J. N., Bevan, H., Dodge, C., & Norvell, A. (2009). *Sources of Metal Contamination in the Coal Creek Watershed, Crested Butte, Gunnison County, Colorado: Part III. Early Spring Flow, April 2007.*

- Scott, D. T., Gooseff, M. N., Bencala, K. E., & Runkel, R. L. (2003). Automated calibration of a stream solute transport model: Implications for interpretation of biogeochemical parameters. *Journal of the North American Benthological Society*, 22(4), 492–510. <https://doi.org/10.2307/1468348>
- Shanklin, B., & Ryan, J. N. (2006). *Sources of Metal Contamination in the Coal Creek Watershed, Crested Butte, Gunnison County, Colorado: Part I: Low Flow, September 2005*.
- Singha, K., & Gorelick, S. M. (2005). Saline tracer visualized with three-dimensional electrical resistivity tomography: Field-scale spatial moment analysis: SPATIAL MOMENT ANALYSIS OF ERT. *Water Resources Research*, 41(5). <https://doi.org/10.1029/2004WR003460>
- Singha, K., Pidlisecky, A., Day-Lewis, F. D., & Gooseff, M. N. (2008). Electrical characterization of non-Fickian transport in groundwater and hyporheic systems. *Water Resources Research*, 44(4). <https://doi.org/10.1029/2008WR007048>
- Singley, J. G., Singha, K., Gooseff, M. N., González-Pinzón, R., Covino, T. P., Ward, A. S., Dorley, J., & Hinckley, E.-L. S. (2022). Identification of hyporheic extent and functional zonation during seasonal streamflow recession by unsupervised clustering of time-lapse electrical resistivity models. *Hydrological Processes*, 36(10), e14713. <https://doi.org/10.1002/hyp.14713>
- Streufert, R., Eakins, W., Hemborg, T., Morgan, M., & Colorado Geological Survey. (1999). *Geology and mineral resources of Gunnison County, Colorado. Denver, Colo. : Colorado Geological Survey, Department of Natural Resources*. <http://hermes.cde.state.co.us/drupal/islandora/object/co:27340/datastream/OBJ/view>
- The Mineral Policy. (1994). Burden of Gilt. *State Legislatures*, 20(6), 6–7.
- Trauth, N., Schmidt, C., Maier, U., Vieweg, M., & Fleckenstein, J. H. (2013). Coupled 3-D stream flow and hyporheic flow model under varying stream and ambient groundwater flow conditions in a pool-riffle system. *Water Resources Research*, 49(9), 5834–5850. <https://doi.org/10.1002/wrcr.20442>
- Trévisan, D., & Perriñez, R. (2016). Coupling catchment hydrology and transient storage to model the fate of solutes during low-flow conditions of an upland river. *Journal of Hydrology*, 534, 317–325. <https://doi.org/10.1016/j.jhydrol.2015.12.058>
- United States Geological Survey. (2016). *Hydrologic Cycle and Interactions*. [https://pubs.usgs.gov/circ/circ1139/htdocs/natural\\_processes\\_of\\_ground.htm](https://pubs.usgs.gov/circ/circ1139/htdocs/natural_processes_of_ground.htm)
- U.S. Geological Survey. (2019). *Specific conductance* (Techniques and Methods No. 9; U.S. Geological Survey Techniques and Methods).

- USEPA. (2020). *First five-year review report for Standard Mine superfund site Gunnison County, Colorado*. U.S. Environmental Protection Agency. <https://semspub.epa.gov/work/08/100007961.pdf>
- Wagener, T., Camacho, L. A., & Wheeler, H. S. (2002). Dynamic identifiability analysis of the transient storage model for solute transport in rivers. *Journal of Hydroinformatics*, 4(3), 199–211.
- Wagner, B. J., & Harvey, J. W. (1997). Experimental design for estimating parameters of rate-limited mass transfer: Analysis of stream tracer studies. *Water Resources Research*, 33(7), 1731–1741. <https://doi.org/10.1029/97WR01067>
- Ward, A. S., Gooseff, M. N., Fitzgerald, M., Voltz, T. J., & Singha, K. (2014). Spatially distributed characterization of hyporheic solute transport during baseflow recession in a headwater mountain stream using electrical geophysical imaging. *Journal of Hydrology*, 517, 362–377. <https://doi.org/10.1016/j.jhydrol.2014.05.036>
- Ward, A. S., Gooseff, M. N., & Singha, K. (2010a). Characterizing hyporheic transport processes—Interpretation of electrical geophysical data in coupled stream–hyporheic zone systems during solute tracer studies. *Advances in Water Resources*, 33(11), 1320–1330. <https://doi.org/10.1016/j.advwatres.2010.05.008>
- Ward, A. S., Gooseff, M. N., & Singha, K. (2010b). Imaging hyporheic zone solute transport using electrical resistivity. *Hydrological Processes*, 24(7), 948–953. <https://doi.org/10.1002/hyp.7672>
- Wentz, D. (1973). Effect of mine drainage on the quality of streams in Colorado, (1971-1972). *Colorado Water Resources Journal*.
- Williams, A. P., Cook, B. I., & Smerdon, J. E. (2022). Rapid intensification of the emerging southwestern North American megadrought in 2020–2021. *Nature Climate Change*, 12(3), Article 3. <https://doi.org/10.1038/s41558-022-01290-z>
- Wlostowski, A. N., Gooseff, M. N., Bowden, W. B., & Wollheim, W. M. (2017). Stream tracer breakthrough curve decomposition into mass fractions: A simple framework to analyze and compare conservative solute transport processes. *Limnology and Oceanography: Methods*, 15(2), 140–153. <https://doi.org/10.1002/lom3.10148>
- Wlostowski, A. N., Gooseff, M. N., & Wagener, T. (2013). Influence of constant rate versus slug injection experiment type on parameter identifiability in a 1-D transient storage model for stream solute transport. *Water Resources Research*, 49(2), 1184–1188. <https://doi.org/10.1002/wrcr.20103>
- Zarnetske, J. P., Haggerty, R., Wondzell, S. M., Bokil, V. A., & González-Pinzón, R. (2012). Coupled transport and reaction kinetics control the nitrate source-sink function of hyporheic zones. *Water Resources Research*, 48(11). <https://doi.org/10.1029/2012WR011894>

- Zhi, W., Li, L., Dong, W., Brown, W., Kaye, J., Steefel, C., & Williams, K. H. (2019). Distinct Source Water Chemistry Shapes Contrasting Concentration-Discharge Patterns. *Water Resources Research*, 55(5), 4233–4251. <https://doi.org/10.1029/2018WR024257>
- Zhi, W., Williams, K. H., Carroll, R. W. H., Brown, W., Dong, W., Kerins, D., & Li, L. (2020). Significant stream chemistry response to temperature variations in a high-elevation mountain watershed. *Communications Earth & Environment*, 1(1), Article 1. <https://doi.org/10.1038/s43247-020-00039-w>

## APPENDIX A

### SUPPORTING FIGURES AND ANALYSES

This section includes additional data collected during both the August and September tracer tests. This additional data was used to better analyze the data presented in the general body of this manuscript. Also included in this section are temporal moment and hysteresis analyses not used in the primary thesis.

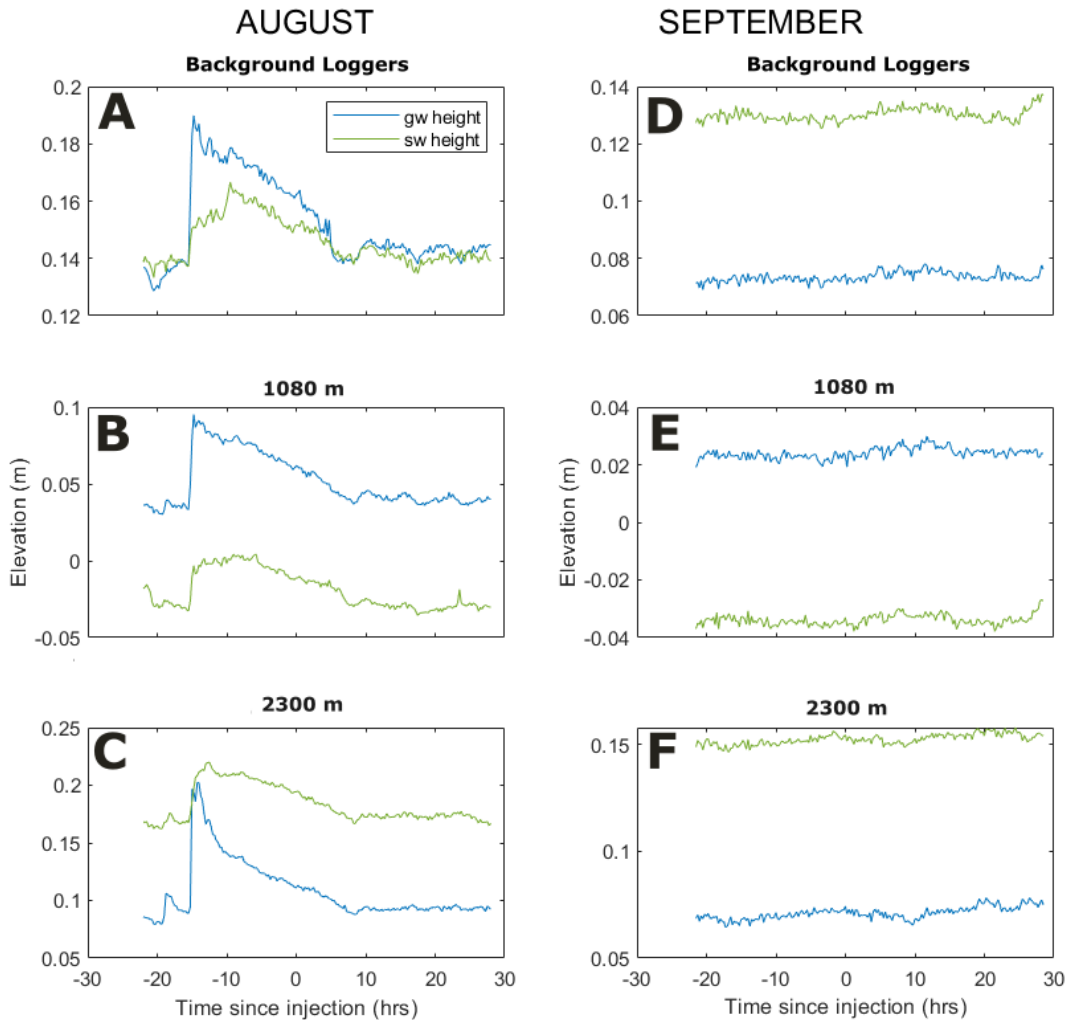


Figure A.1: Select data from the (A-C) August and (D-F) September 2022 tracer injection experiments showing the SW and GW relative elevation as measured (A, D) immediately upstream of the injection site, and (B, E) 1080m and (C, F) 2300m downstream of the injection site —with a pressure transducer—over time since injection start.

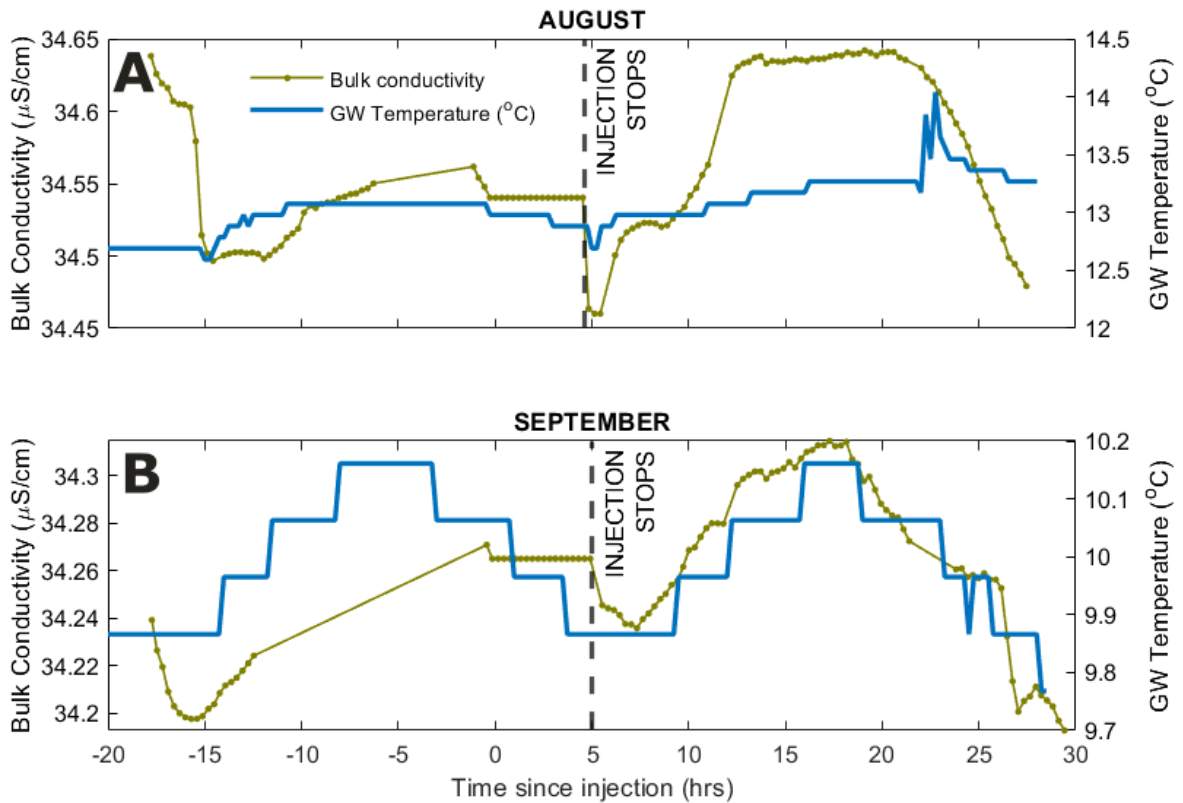


Figure A.2: The GW temperatures and bulk conductivities during the (A) August and (B) September tracer tests over time since the start of injection.

A hysteresis analysis/plot of fluid and bulk conductivities aids in the characterization of solute transport between mobile and less-mobile zones. Essentially, the hysteresis plots show the injection and flush cycle. The goal with of this work was to quantify the exchange rate between the less (bulk) and more mobile (fluid) zones of the stream and estimate parameters of the hyporheic zone following Briggs et al. (2014); however, given limited variability in the bulk data, we were unable to make use of this analysis.

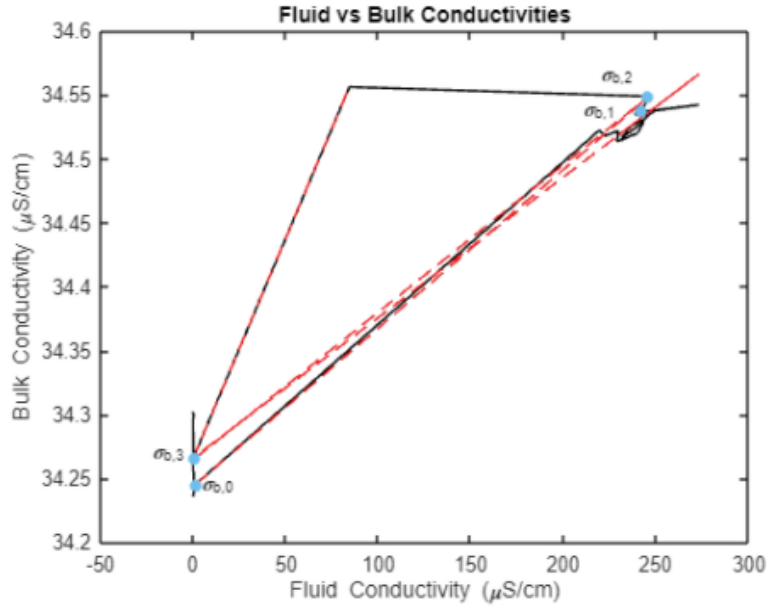


Figure A.3: Hysteresis patterns measured during the September tracer experiment 100m downstream from the injection site. This shows the associated hinge points used to determine  $\beta$  from the rising limb (injection phase) as outlined by Briggs et al. (2014).

The calculated  $\beta$ , the distribution coefficient, values are in the range of 0.02 to 2, given the equations from Briggs et al., (2014; Figure A.4). This low  $\beta$  values indicate little solute distribution. This might be an erroneous hysteresis plot given the limited range of bulk conductivity (34.25 – 34.55  $\mu\text{S}/\text{cm}$ ).

$$\beta = m_{0,2}/m_{0,1} - 1,$$

$$\beta = m_{0,2}/m_{2,3} - 1,$$

$$\beta = \frac{\sigma_{b,2} - \sigma_{b,1}}{\sigma_{b,1} - \sigma_{b,0}},$$

$$\beta = \frac{\sigma_{b,3} - \sigma_{b,0}}{\sigma_{b,2} - \sigma_{b,3}}.$$

Figure A.4: The equations presented by Briggs et al. (2014) on how to yield estimates of the ratio of less mobile to mobile porosities ( $\beta$ ) using the graphical method.

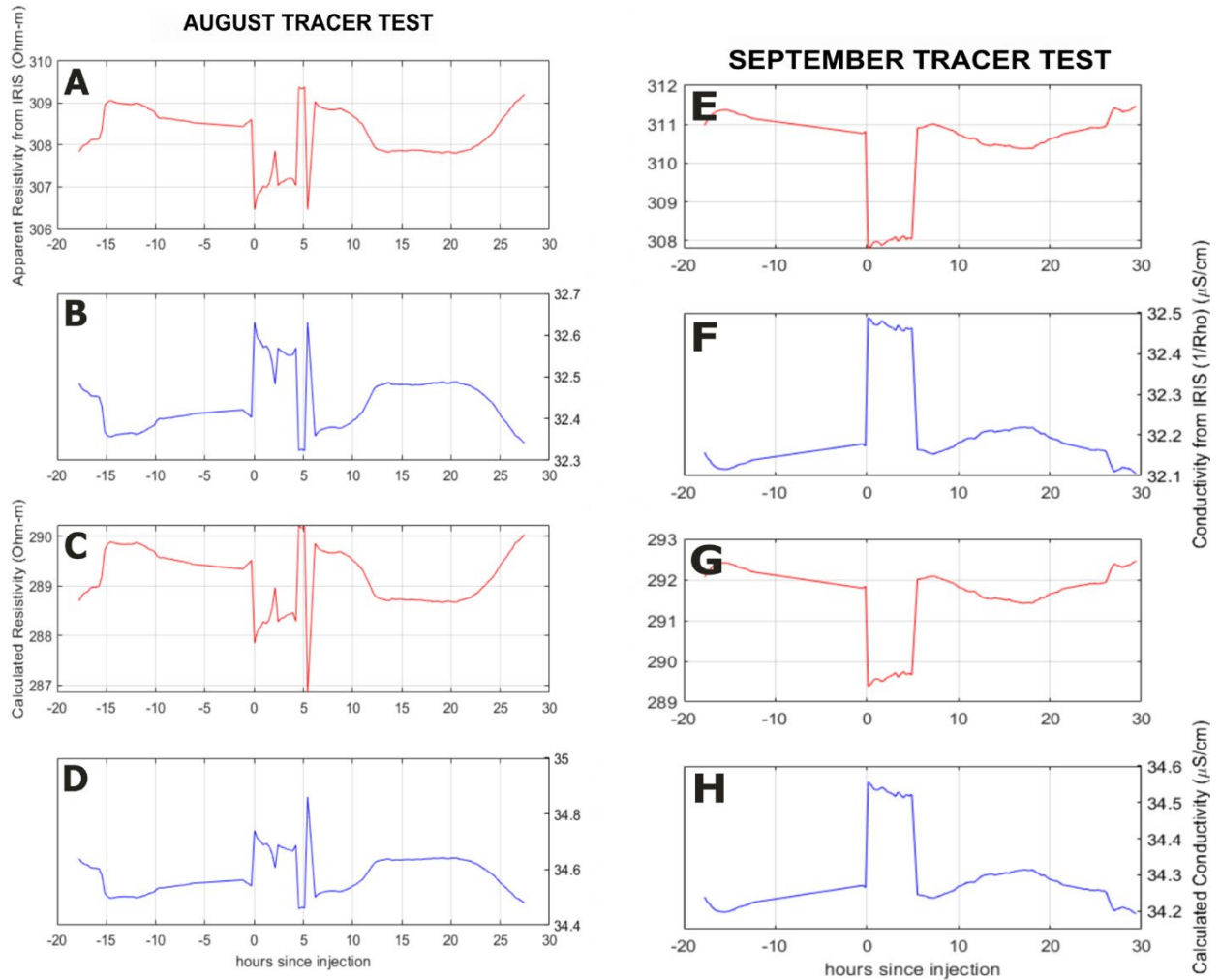


Figure A.5: Select data used for processing the ER data collected during the (A-D) August tracer test and the (E-H) September tracer test, including (A, E) measured apparent resistivity, the (B, F) conductivity as measured by the IRIS instrument, the (C, G) calculated resistivity and (D, H) calculated conductivity.

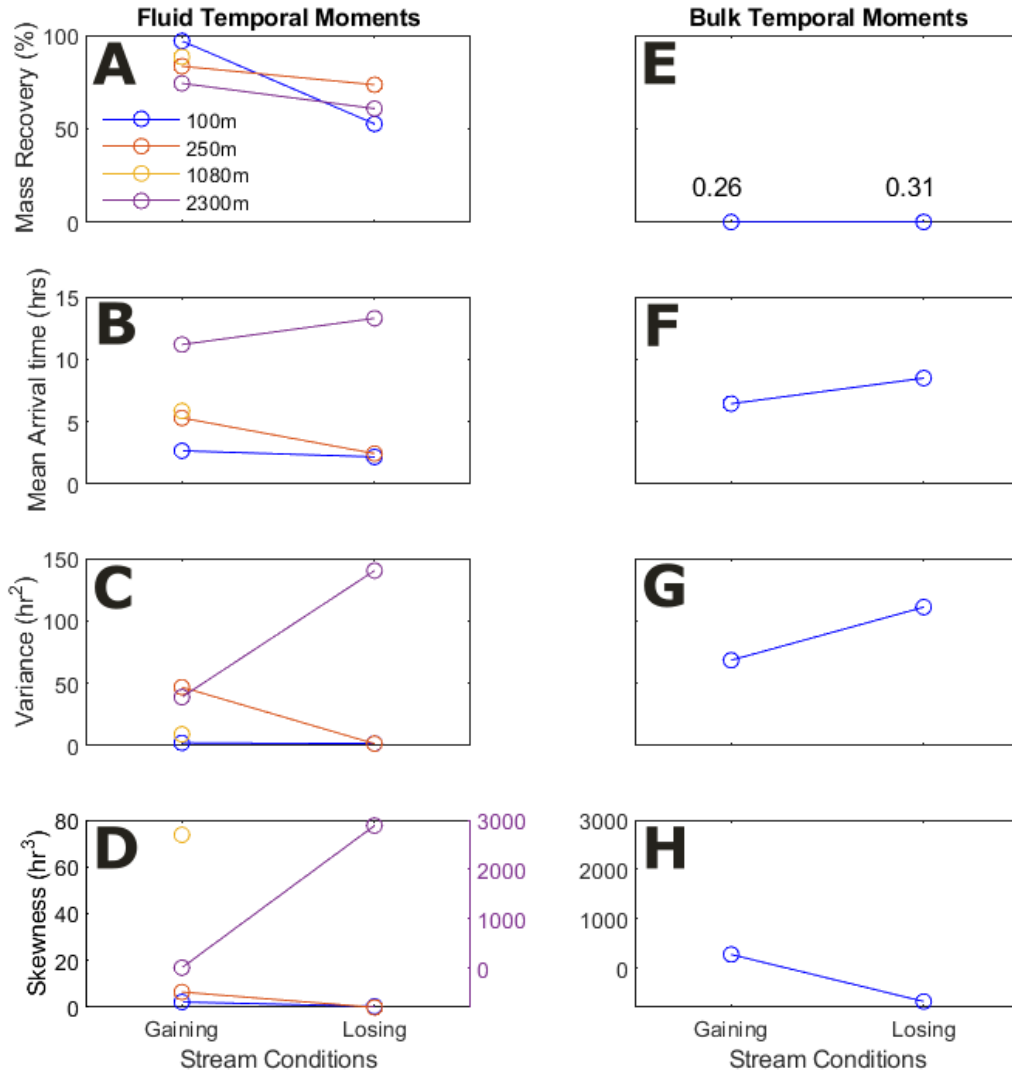


Figure A.6: Temporal moments were calculated based on the fluid conductivity at the four downstream locations (100, 250, 1080 and 2300 m) and based on bulk conductivity at 100 m downstream from the injection, during two different baseflow conditions (gaining in August and losing in September). The temporal moments were used to determine (A, E) percent mass recovery (%), (B, F) mean arrival time (hr), (C, G) temporal variance ( $hr^2$ ), and (D, H) skewness ( $hr^3$ ). Note the skewness values shown in purple in the D subplot correspond to the 2300 m location. Additionally, skew values for each downstream location were not truncated to represent equal times after injection start but were taken according to each time length as shown in Figure 2.6.

Temporal moments were also used to estimate mean arrival times, temporal variance and skewness for the August and September tracer experiments at each downstream logger location (Figure A.6). The mean arrival time obtained from the fluid temporal moments (Figure A.6B) was

found to increase with increasing downstream distance as expected, but it appeared to decrease when stream conditions switched from gaining to losing for 100m and 250m downstream locations (Figure A.6B and A.6F). A slight increase in the mean arrival time was observed when the stream conditions changed from gaining to losing at the 2300m downstream location (Figure A.6B). In contrast, the mean arrival time observed in the bulk conductivity data was almost doubled between tests, and it increased during stream losing conditions (Figure A.6F).

The estimated variance of the BTCs shows no correlation with the streamflow regime (i.e., losing or gaining), given the limited head data collected during this experiment and the number of times the experiment was repeated. The fluid specific conductivity variance remained nearly the same at 100m downstream but decreased at 250m and increased at 2300m when stream changed from gaining to losing (Figure A.6C). There were no fluid data collected at 1080m during the September tracer test, so no comments on any changes between losing and gaining conditions can be made. The bulk specific conductivity variance measured at 100m downstream by the ER survey also was higher during losing conditions than gaining conditions, but no other definitive correlations were observed.

Similar to the variance, the skewness or the tailing/asymmetry of the BTCs does not show correlation with the stream flow regime. Skewness decreased as the stream changed from localized gaining to losing at the 100 and 250m locations (Figure A.6D). For the fluid specific conductivity, the skewness increased with distance from the injection point during localized gaining conditions, with the exception for the collected 1080m data. The highly skewed fluid BTC during localized losing stream conditions at 2300m (Figure A.6D) would indicate an increase in dead zones/transient storage compared to the upstream locations (i.e., 100, 250, 1080m), which would conceptually be plausible given the increased flowpath distance. But during

localized gaining conditions in September, the 2300m BTC was the least skewed compared to the other measurement locations. This would imply the stream condition affects the fluid BTC skewness, but this correlation is difficult to determine decisively given the limited number of tracer tests performed. The mean arrival time of the tracer was minimally changed between gaining versus losing stream conditions, which also makes some sense given similar streamflows. However, the variance and skewness did not reveal a definitive trend based on downstream distance from the injection point or based on the stream conditions. The notable increase in variance and skewness at 2300m from gaining August to losing September stream conditions (Figure A.6B-C) indicates the tracer might have been retained more via instream transient storage during losing conditions, whereas the August tracer test exhibited a greater possibility for SW-GW connectivity—based on ER data—and greater potential for transient storage in the hyporheic zone based on the flow regime.

The bulk conductivities (Figure 1E) show a mass recovery of 0.26 and 0.31% during a gaining stream and losing stream, respectively. Such underestimates are common in geophysical data analysis (e.g., Singha and Gorelick, 2005). Bulk conductivity skewness was collected only at 100m with the ER survey, and generally showed a decrease from the August to September test when stream conditions changed from gaining to losing (Figure A.6H). Skewness during losing conditions showed a highly negative value, which indicates a late bulk arrival of the solute. The highly negative skewness is likely a result of the second increase in bulk conductivity observed at ~10 hrs after the injection started (Figure 2.5A). In general, bulk skewness values are low, indicating that there is little to no exchange between the stream and the hyporheic zone under these conditions.

## APPENDIX B

### ER INVERSIONS FROM TRACER TESTS

The ER inversions generated with ResIPy during both tracer tests are presented in the following sections.

#### **B.1 August Electrical Resistivity Tracer Inversions**

The inversion results as output by ResIPy for the entirety of the tracer test performed in August are presented in the supplemental document, `supplemental_data.docx` under the “August Electrical Resistivity Tracer Inversions” section. These difference inversions are cross-sections where the stream is flowing out of the page and the difference/change in resistivity is shown from a background condition. The warmer coloring represents a decrease in resistivity. The first inversion is immediately after the tracer injection begins. The time and the root-mean-square (RMS) misfit are shown for each inversion. The misfit is a percentage that shows how well the inversion model fits the actual data. An RMS misfit of 1.00 is ideal.

#### **B.2 September Electrical Resistivity Tracer Inversions**

The figures and data presented in supplemental data “September Electrical Resistivity Tracer Inversions” are the inversion results as output by ResIPy for the entirety of the tracer test performed in September, with identical settings to those described in sections B.1.

#### **B.3 Tracer Test Data From 2300m Injection Site**

The following section contains data from a tracer test performed at another location along Coal Creek that is known as “Coal-20”. Coal-20 is the same as the location 2300m downstream from the injection site reported in the main components of this manuscript. The inversions for the August Coal-20 tracer test are presented in `supplemental_data.docx` section, “September Electrical Resistivity Tracer Inversions at 2300m Injection Site”. The calculated apparent resistivity (Figure B.1C)—corrected with a geometric factor—did not follow the same trends as

the raw data (i.e., data output by the IRIS directly; Figure B.1A) and therefore the screening process would have been too time consuming for the scope of this work.

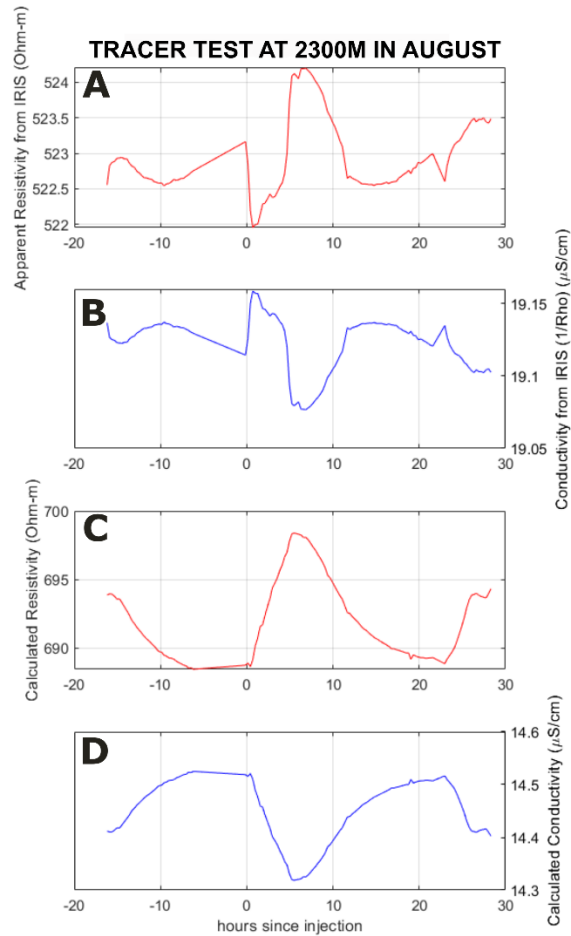


Figure B.1: A) From top to bottom: for the August tracer (A) measured apparent resistivity and the (B) conductivity as measured by the IRIS instrument are compared to the (C) calculated resistivity and (D) calculated conductivity.

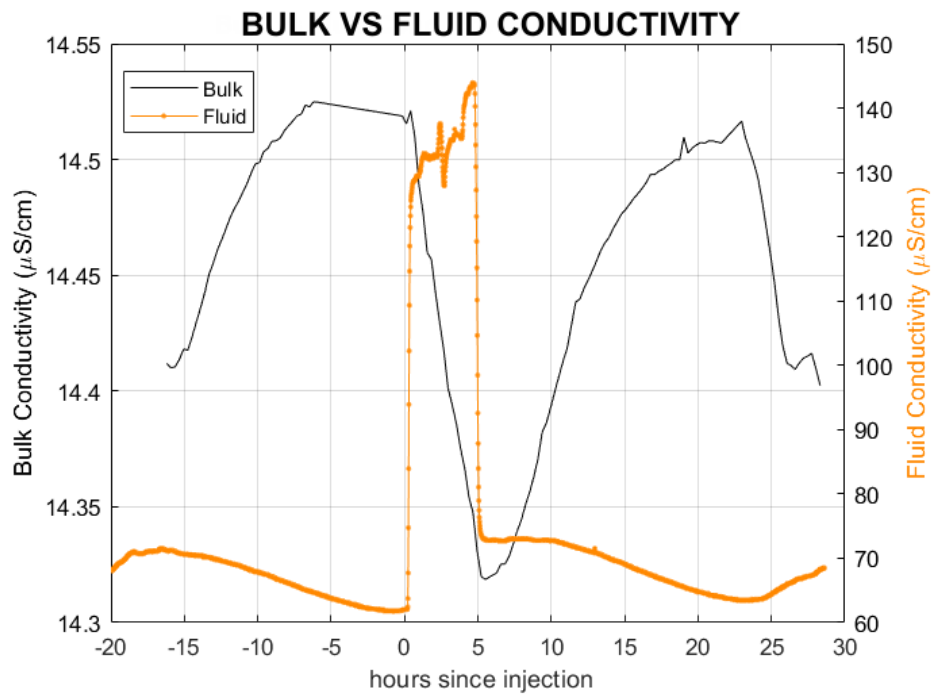


Figure B.2: A) The bulk versus fluid conductivity for the August tracer test performed 2300m downstream.

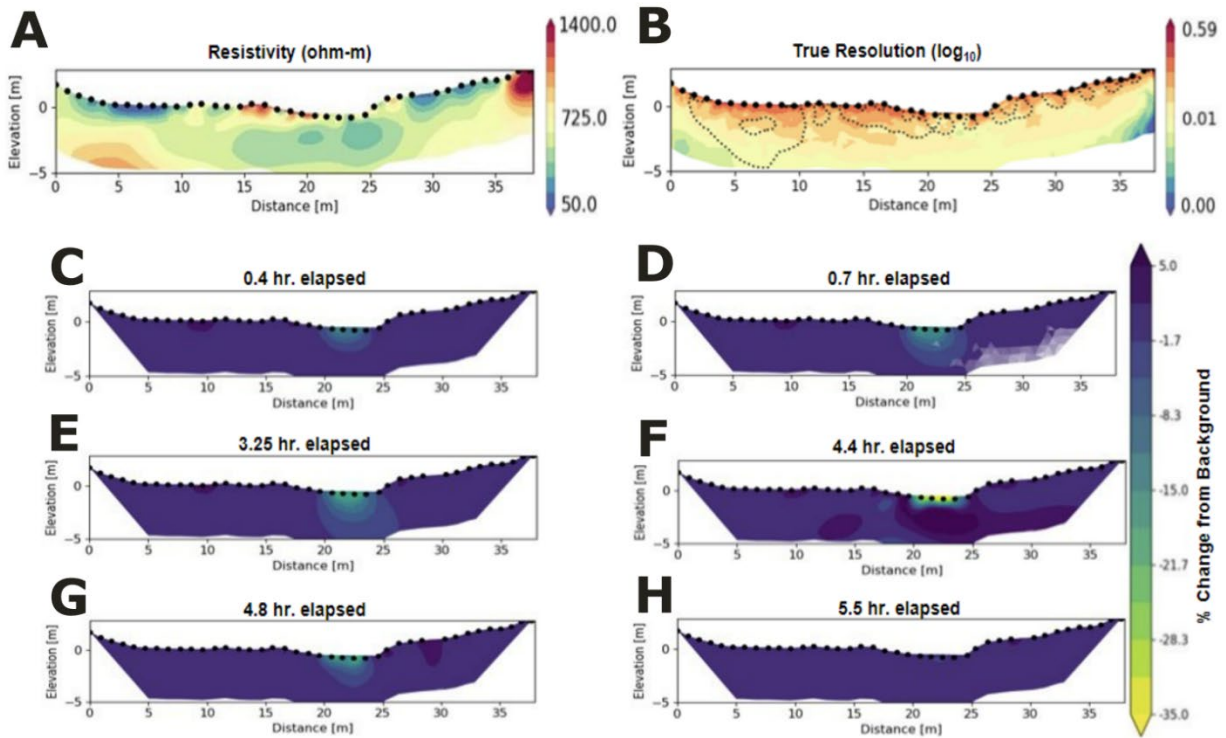


Figure B.3: Inversion models from August at the 2300m location are presented as cross-sections transverse to the stream with flow directed out of the page. A) The pre-injection electrical resistivity model. B) The diagonal of the true resolution matrix, which measures how well the data and the model parameters are resolved i.e., any resolution value close to 1 would indicate equal predicted and measured values. The dashed line is the depth of investigation (DOI). C–H) Selected ER inversions for the tracer injection test (see Appendix B for all images) as percent changes from the pre-injection electrical resistivity model at time elapsed after beginning the conservative solute injection. C–G) Decrease in bulk resistivity in the subsurface due to tracer presence. H) Tracer is flushed from the subsurface.